












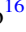









# Reflectivity of Venus's Dayside Disk During the 2020 Observation Campaign: Outcomes and Future Perspectives

Yeon Joo Lee<sup>1,2</sup> , Antonio García Muñoz<sup>3</sup> , Atsushi Yamazaki<sup>4,5</sup> , Eric Quémerais<sup>6</sup> , Stefano Mottola<sup>1</sup> , Stephan Hellmich<sup>1,7</sup> , Thomas Granzer<sup>8</sup>, Gilles Bergond<sup>9</sup>, Martin Roth<sup>8</sup> , Eulalia Gallego-Cano<sup>10</sup> , Jean-Yves Chaufray<sup>6</sup>, Rozenn Robidel<sup>6</sup>, Go Murakami<sup>4</sup>, Kei Masunaga<sup>4</sup> , Murat Kaplan<sup>11</sup>, Orhan Erece<sup>11</sup>, Ricardo Hueso<sup>12</sup> , Petr Kabáth<sup>13</sup> , Magdaléna Špoková<sup>13,14</sup>, Agustín Sánchez-Lavega<sup>12</sup> , Myung-Jin Kim<sup>15</sup> , Valeria Mangano<sup>16</sup> , Kandis-Lea Jessup<sup>17</sup>, Thomas Widemann<sup>18</sup>, Ko-ichiro Sugiyama<sup>19</sup>, Shigeto Watanabe<sup>20</sup> , Manabu Yamada<sup>21</sup> , Takehiko Satoh<sup>4</sup> , Masato Nakamura<sup>4</sup>, Masataka Imai<sup>22</sup> , and Juan Cabrera<sup>1</sup> 

<sup>1</sup>DLR Institute of Planetary Research, Berlin, Germany

<sup>2</sup>Pioneer Research Center for Climate and Earth Science, Institute for Basic Science (IBS), Daejeon 34126, Republic of Korea; [yeonjoollee@ibs.re.kr](mailto:yeonjoollee@ibs.re.kr)

<sup>3</sup>AIM, CEA, CNRS, Université Paris-Saclay, Université de Paris, Gif-sur-Yvette, France

<sup>4</sup>Institute of Space and Astronautical Science (ISAS/JAXA), Sagami-hara, Japan

<sup>5</sup>Graduate School of Science, University of Tokyo, Tokyo, Japan

<sup>6</sup>LATMOS-OVSQ, Université Versailles Saint-Quentin, Guyancourt, France

<sup>7</sup>Laboratory of astrophysics, École Polytechnique Fédérale de Lausanne (EPFL), Observatoire de Sauverny, 1290 Versoix, Switzerland

<sup>8</sup>Leibniz-Institute for Astrophysics Potsdam (AIP), Potsdam, Germany

<sup>9</sup>CAHA, Almeria, Spain

<sup>10</sup>IAA Granada, Spain

<sup>11</sup>Akdeniz Univ., Antalya, Turkey

<sup>12</sup>Dpt. Física Aplicada, Escuela de Ingeniería de Bilbao, Universidad del País Vasco UPV/EHU, Bilbao, Spain

<sup>13</sup>Astronomical Institute AS CR, Ondřejov, Czech Republic

<sup>14</sup>Masaryk University, Department of theoretical physics and astrophysics, Kotlářská 2, 611 37, Brno, Czech Republic

<sup>15</sup>Korea Astronomy and Space Science Institute (KASI), Daejeon, Republic of Korea

<sup>16</sup>INAF-IAPS (Institute for Astrophysics and Planetology from Space), Rome, Italy

<sup>17</sup>Southwest Research Institute, Boulder, CO, USA

<sup>18</sup>Observatoire de Paris-PSL & Université Paris-Saclay, LESIA—UMR CNRS, Meudon, France

<sup>19</sup>Matsue National College of Technology, Matsue, Japan

<sup>20</sup>Space Information Center, Hokkaido Information University, Ebetsu, Japan

<sup>21</sup>Planetary Exploration Research Center (PERC), Narashino, Japan

<sup>22</sup>Kyoto Sangyo University, Kyoto, Japan

Received 2022 April 9; revised 2022 July 25; accepted 2022 July 26; published 2022 September 14

## Abstract

We performed a unique Venus observation campaign to measure the disk brightness of Venus over a broad range of wavelengths in 2020 August and September. The primary goal of the campaign was to investigate the absorption properties of the unknown absorber in the clouds. The secondary goal was to extract a disk mean SO<sub>2</sub> gas abundance, whose absorption spectral feature is entangled with that of the unknown absorber at ultraviolet wavelengths. A total of three spacecraft and six ground-based telescopes participated in this campaign, covering the 52–1700 nm wavelength range. After careful evaluation of the observational data, we focused on the data sets acquired by four facilities. We accomplished our primary goal by analyzing the reflectivity spectrum of the Venus disk over the 283–800 nm wavelengths. Considerable absorption is present in the 350–450 nm range, for which we retrieved the corresponding optical depth of the unknown absorber. The result shows the consistent wavelength dependence of the relative optical depth with that at low latitudes, during the Venus flyby by MESSENGER in 2007, which was expected because the overall disk reflectivity is dominated by low latitudes. Last, we summarize the experience that we obtained during this first campaign, which should enable us to accomplish our second goal in future campaigns.

*Unified Astronomy Thesaurus concepts:* Venus (1763); Atmospheric clouds (2180); Planetary science (1255); Solar system astronomy (1529); Planetary atmospheres (1244); Observational astronomy (1145)

## 1. Introduction

As the third-brightest object in the sky after the Sun and the Moon, the scientific observations of Venus started early. A century ago, ground-based observations discovered the presence of dark patches in ultraviolet (UV) images of the planet (Wright 1927; Ross 1928). The chemical that produces the dark patches on the planet is characterized by broad absorption that

extends from the UV to the visible wavelengths. The identity of such a chemical remains elusive, and the substance is still called the “unknown absorber” (Barker et al. 1975; Pollack et al. 1980; Zasova et al. 1981; Mills et al. 2007; Titov et al. 2018). Recent studies have suggested that the unknown absorber may be OSSO or S<sub>2</sub>O, which explains the observed UV spectrum (Pérez-Hoyos et al. 2018). According to photochemical model calculations (Krasnopolsky 2018) and glory observation analysis (Petrova 2018), the unknown absorber could also be iron chloride. There are more



Original content from this work may be used under the terms of the [Creative Commons Attribution 4.0 licence](https://creativecommons.org/licenses/by/4.0/). Any further distribution of this work must maintain attribution to the author(s) and the title of the work, journal citation and DOI.

candidates, such as  $S_x$ ,  $Cl_2$ ,  $SCl_2$ , etc. (Mills et al. 2007). Recently, iron-bearing microorganisms have also been proposed (Limaye et al. 2018).

The absorption spectrum of the unknown absorber was reported to have its maximum at 340 nm, with an FWHM of 140 nm, according to the MESSENGER/MASCS data (Pérez-Hoyos et al. 2018). But considering the limited spectral range of the MESSENGER/MASCS data—300–1500 nm—the spectral properties of the unknown absorber at  $\lambda < 300$  nm were not accessed, remaining undefined. Spectral data at such short wavelengths were acquired by the SPICAV spectrometer on board Venus Express, covering the 170–320 nm range with its UV channel. In order to explain the data taken by SPICAV’s UV channel, Marcq et al. (2011, 2020) postulated the presence of an unknown absorber in the form of a cloud aerosol, in addition to a pure sulfuric acid aerosol. The putative absorber would explain the absorption shortward of 300 nm. These previous studies suggest that the unknown absorber remains effective at wavelengths from  $\sim 200$  nm (Marcq et al. 2020) to  $\sim 600$  nm (Pérez-Hoyos et al. 2018). These observations were done at different times, and with different viewing geometries, so their data cannot be directly combined to understand the spectral properties of the unknown absorber over the entire UV–visible wavelength range. To elucidate such properties, it is clear that additional observations should be made over a broader range of wavelengths, such as those done by the STIS spectrometer on board the Hubble Space Telescope over 200–600 nm (Jessup et al. 2020).

The UV observations are also useful for retrieving abundances of trace gases near the cloud-top level. For example,  $SO_2$  bands are located near 215 and 280 nm, the SO band near 215 nm, and the  $O_3$  band near 250 nm (Esposito et al. 1988; Na et al. 1990; Belyaev et al. 2012; Jessup et al. 2015; Marcq et al. 2019, 2020). Their abundances and variations are important for understanding photochemical processes in the atmosphere (Mills et al. 2007; Titov et al. 2018), including their interaction with the unknown absorber (Marcq et al. 2013, 2020; Lee et al. 2015a, 2019). However, without high spectral resolution, the interpretation is complicated by the overlap of the bands and by the absorption of the unknown absorber. A further complication would be represented by the presence of an additional species,  $H_2S$ , near the cloud-top level, as suggested by Bierson & Zhang (2020). This contribution, not considered in previous studies (Na et al. 1990; Belyaev et al. 2012; Jessup et al. 2015), is characterized by a UV band near 215 nm that overlaps those of the SO and  $SO_2$  gases.

Significant temporal variations of the unknown absorber and  $SO_2$  gas abundance have been reported over both short- and long-term periods (Del Genio & Rossow 1982; Esposito et al. 1988; Del Genio & Rossow 1990; Marcq et al. 2013, 2020; Lee et al. 2015a, 2019, 2020; Imai et al. 2019). In terms of disk-integrated UV brightness, short-term variations indicate the presence of global-scale atmospheric waves with a periodicity of 4–5 days (Del Genio & Rossow 1982; Lee et al. 2020), whose amplitudes are changing with time (Del Genio & Rossow 1990; Imai et al. 2019; Lee et al. 2020). Changes in the disk-integrated UV brightness over timescales of decades can impact the solar energy deposition in the atmosphere, because almost half of the solar heating at the cloud-top atmosphere is caused by the unknown absorber (Crisp 1986; Lee et al. 2015b). The latter can lead to considerable changes in global-

scale circulation and zonal wind speeds (Lee et al. 2019). Intriguingly, the UV brightness variations are correlated with the  $SO_2$  gas abundance near the cloud-top level (Lee et al. 2015a, 2019; Marcq et al. 2020). That connection is key to understanding the photochemical processes that affect cloud formation (Mills et al. 2007) and the impact of possible volcanic outgassing on the atmosphere. We need further data to investigate the relationship between the sulfur-related gaseous abundance and the unknown absorber. That was the main motivation for the Venus dayside observation campaign that we performed in 2020.

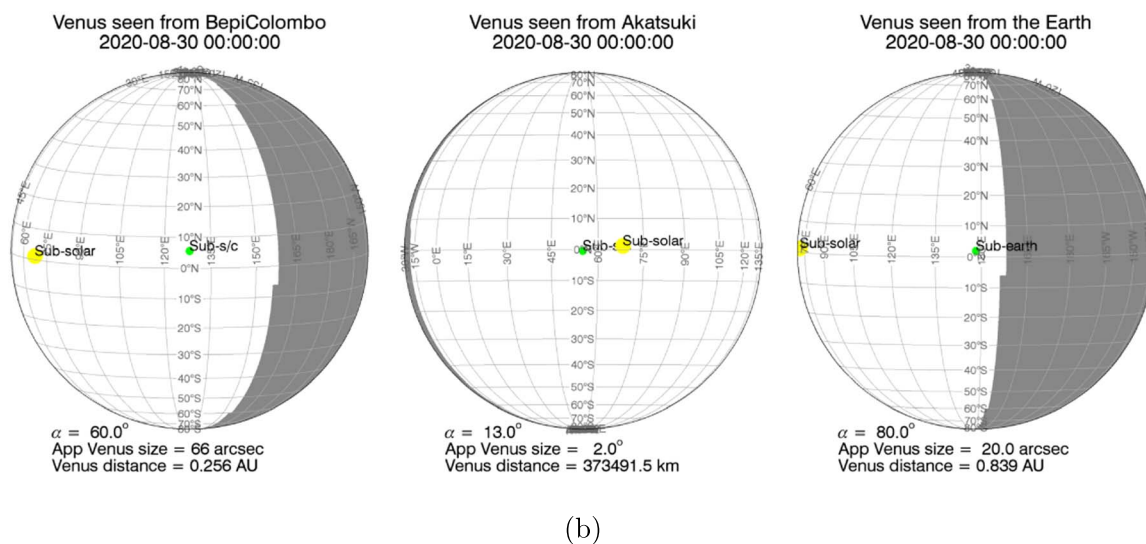
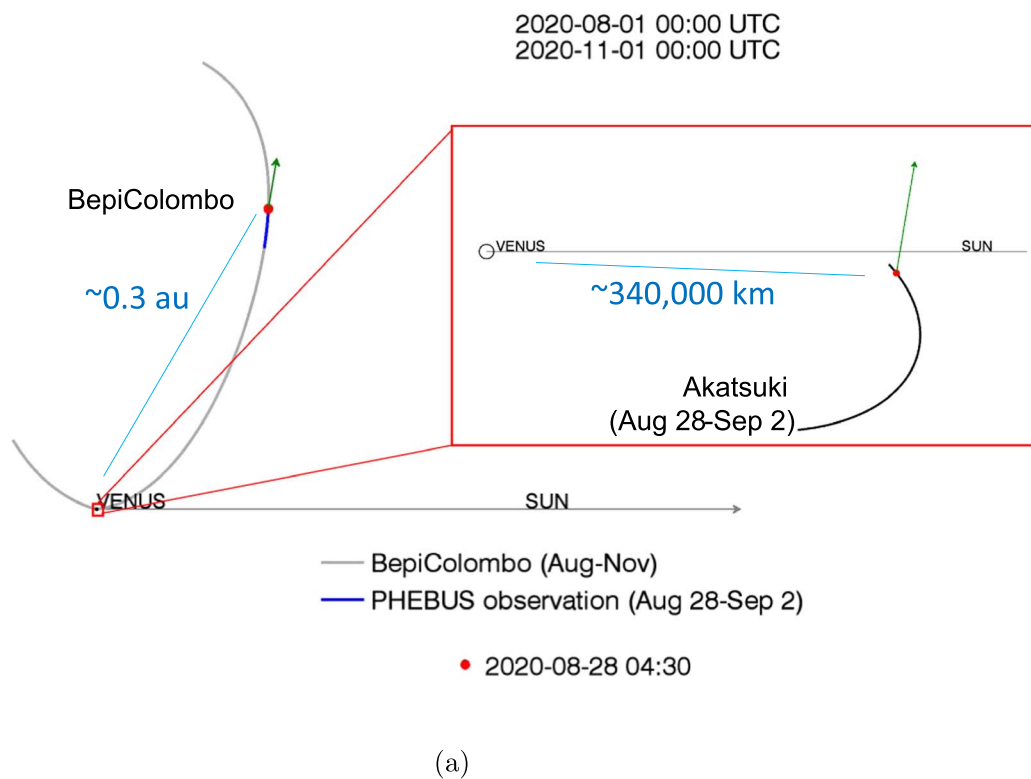
As our campaign measures the disk-integrated spectral brightness, the results will be useful for comparison with spatially unresolved data acquired by future exoplanet imaging investigations. For example, we now know that measuring the planet’s brightness at more than one phase angle could be a valuable strategy for identifying Venus-like clouds at exoplanets, if they exist, with future direct imaging telescopes (Carrion-González et al. 2020, 2021). In this manuscript, we describe the campaign (Section 2), explain the data reduction (Section 3), the atmospheric modeling (Section 4), and the data analysis (Section 5), and offer our lessons learned for the purpose of planning future campaigns (Section 6).

## 2. Observations

In 2020 August and September, we performed the Venus dayside observation campaign from three locations in the solar system: the Akatsuki Venus orbiter, the BepiColombo Mercury orbiter, on its cruise phase toward Mercury, and the Earth (via the Earth-orbiting Hisaki spacecraft and ground-based telescopes; Figure 1(a)). JAXA’s Venus orbiter Akatsuki operates from a highly elliptical equatorial orbit. The onboard UV camera (UltraViolet Imager: UVI) has monitored Venus since the orbit insertion in 2015 December (Nakamura et al. 2016). ESA-JAXA’s BepiColombo conducted faraway Venus observations from a distance of 0.3 au in the period 2020 August 28–September 2, when Venus was within the field of view (FOV) of the onboard UV spectrometer (PHEBUS; Mangano et al. 2021). While these two spacecraft were operating, ground-based telescopes were in a good position to observe Venus for more than an hour right before sunrise. Three telescopes of the Calar Alto observatory (CAHA) joined the campaign and conducted the Venus observations: the CAHA 1.23 m DLR-MKIII CCD camera,<sup>23</sup> the CAHA 2.2 m PlanetCam camera (Mendikoa et al. 2016), and the CAHA 3.5 m Potsdam Multi-Aperture Spectrophotometer (PMAS; Roth et al. 2005). TÜBİTAK National Observatory’s T100 CCD camera<sup>24</sup> and the STELLA 1.2 m telescope’s Wide-Field STELLA Imaging Photometer (WiFSIP; Strassmeier et al. 2010) acquired images, and the Perek telescope’s Ondřejov Echelle Spectrograph (OES; Kabáth et al. 2020) acquired spectra. JAXA’s Earth-orbiting Hisaki space telescope also obtained Venus data in the extreme UV (EUV) range, with the EXCEED spectrometer (Yoshikawa et al. 2014), which has been used to detect the airglow of Venus (Nara et al. 2018). The EUV data can help to examine possible faint dayside reflection by the upper haze of Venus, thanks to their long exposure time over

<sup>23</sup> [http://www.caha.es/CAHA/Instruments/IA123/DLR\\_Observation\\_guide\\_v1.11.pdf](http://www.caha.es/CAHA/Instruments/IA123/DLR_Observation_guide_v1.11.pdf)

<sup>24</sup> <https://tug.tubitak.gov.tr/en/teleskoplar/t100-teleskope>



**Figure 1.** Overview of the campaign observations. (a) The relative locations of the observation facilities from Venus. The green arrows indicate the direction toward Earth from the spacecraft. The gray curve of BepiColombo indicates the trajectory from 2020 August to November, and the blue curve highlights the location during the campaign period (August 28–September 2). Akatsuki’s trajectory between August 28 and September 2 is shown in the enlarged red box. The red dots are the locations of the spacecraft on August 28 at 04:30 UT. (b) Viewing geometries of Venus from Akatsuki, BepiColombo, and Earth on August 30. The day/night areas are indicated with the white/gray areas over the disk. The solar phase angle ( $\alpha$ ), the apparent size of Venus, and the distance between the planet and observers are listed at the bottom. The subsolar and the subobserver points are indicated with the yellow and green dots, respectively.

10 days. Table 1 shows the complete list of facilities, with observation dates and wavelength ranges.

The uniqueness of this campaign is the broad spectral coverage for observations of the Venus disk, which extends from 52 to 1700 nm, and which cannot be acquired by a single instrument. We took advantage of the spectral overlap between the instruments, which could be used to combine individual

spectral pieces of the brightness. For example, EXCEED and PHEBUS overlap at 145–148 nm; PHEBUS and UVI at 283 nm; UVI, the ground-based *U* band, and PMAS at 365 nm; and the ground-based *B* band and PMAS at 445 nm.

Half of the facilities acquired data of sufficient quality for scientific analysis, but not the others (Table 1). There were four problems for the latter. (1) The first problem was the

**Table 1**  
Summary of the Campaign Observations

Location (1)	Facility/Inst. (2)	Type <sup>a</sup> (3)	Spectral Range (nm) (4)	Date (5)	Status and Section (6)
Space (Venus orbit)	Akatsuki/UVI	I	283, 365	Regular monitoring	Success, Section 3.1
Space (interplanetary)	BepiColombo/PHEBUS	S	145–315, 402, 423	Aug 28–Sep 2	Insufficient for analysis, Section 3.2 (not used)
Space (Earth orbit)	Hisaki/EXCEED	S	52–148	Aug 21–Sep 3	Success for relative analysis (not used)
Spain	CAHA1.23/DLR-MKIII	I	<i>BVRI</i> bands	Aug 21–28	Success, Section 3.3
Spain	CAHA2.2/PlanetCam	I	380–1700	Aug 28–31	Insufficient for analysis (not used)
Spain	CAHA3.5/PMAS	I and S	364–457 ( $d\lambda = 0.28$ nm)	Aug 27–30	Success for relative analysis, Section 3.5
Turkey	TUG/T100	I	<i>UBV</i> bands	Aug 25–Sep 2	Insufficient for analysis (not used)
Spain (Tenerife)	STELLA/WiFSIP	I	<i>U</i> band	Aug–Nov	Success, Section 3.4
Czech Republic	Perek telescope/OES	S	375.3–919.5	Aug 21–Sep 2	Insufficient for analysis (not used)

**Note.** List of acronyms—UVI: UltraViolet Imager; PHEBUS: Probing of Hermean Exosphere By Ultraviolet Spectroscopy; EXCEED: EXtreme ultraviolet spectroScope for Exospheric Dynamics; CAHA: Calar Alto Observatory; PMAS: Potsdam Multi-Aperture Spectrophotometer; TUG: TÜBİTAK National Observatory; WiFSIP: Wide-Field STELLA Imaging Photometer; OES: Ondřejov Echelle Spectrograph.

<sup>a</sup> I: Image; S: Spectrum.

uncertainties in the pointing that occurred during the data acquisition for PHEBUS and EXCEED. Narrow-slit spectrometers require a high accuracy of spacecraft attitude control. The Venus observations by BepiColombo were in fact part of the performance tests on the cruise phase, and it turned out that the pointing accuracy was not always as good as planned. Hisaki gradually saw such control deteriorating with aging. Regardless of this problem, both the PHEBUS and the EXCEED data could have been sufficient for relative spectral analysis. But the PHEBUS data had an additional issue; their effective area turned out not to be well defined for scientific analysis (Section 3.2). Consequently, the EXCEED data could not be used, as a data comparison was not possible at the overlapping wavelengths (145–148 nm). Also, spectral comparison of the reflected daylight between EXCEED and PHEBUS may not be possible even in future, because the exposure time of PHEBUS cannot be as long as that of EXCEED. (2) The second problem was the photometric calibration of the ground-based measurements, which required particular care. To define the telluric extinction coefficients accurately, the CAHA1.23 DLR-MKIII camera frequently interspersed measurements of reference stars with those of Venus (Section 3.3), and the STELLA WiFSIP measured a reference star continuously until Venus rose sufficiently high to acquire data (Section 3.4). However, this was not the case for the other facilities, such as the CAHA2.2 PlanetCam, whose frequency of reference star observations turned out to be insufficient for photometric analysis under variable sky conditions. (3) The third problem was caused by the difficulties in defining an optimal aperture size in the CCD aperture photometry analysis. The TUG T100 data suffered from this problem, which may have been exacerbated by the brightness of Venus. (4) Finally, the Perek OES measurements are not used in this study, because its 2'' width slit is likely on the morning terminator (the center of the 20'' diameter Venus disk).

The Venus observations were conducted in three solar phase angle ( $\alpha$ ) ranges, as shown in Figure 1(b). Near the end of August,  $\alpha$  was 60° for PHEBUS, 0°–40° for UVI, and ~80° from the Earth. In this manuscript, we investigate the spectral features of the entire Venus disk at  $\alpha = 80^\circ$ . To that end, we approximately corrected all the observations at other phase angles to form equivalent observations at  $\alpha = 80^\circ$ . In the future, we plan to investigate the solar phase angle dependence

of Venus's brightness (Lee et al. 2021) over a broad spectral range by repeating similar campaigns at multiple epochs.

### 3. Data

Details of the data acquisition and calibrations are described in this section for each instrument.

#### 3.1. Akatsuki/UVI

UVI has two filters, centered at 283 and 365 nm (Yamazaki et al. 2018). The 365 nm wavelength is to detect the absorption by the unknown absorber, and the 283 nm wavelength is located near the center of a SO<sub>2</sub> band. In the regular observation mode, UVI obtains Venus images via the two filters, every 2 hr, from a highly elliptical equatorial orbit. We selected images with complete coverage of the Venus dayside between 2015 December 7 and 2021 March 31. Some known artifact images are excluded from the data set.

In this analysis, we used two flat fields; the first flat field was measured in a laboratory, before the launch (Yamazaki et al. 2018), and a second, new, flat field was prepared with the diffuser images acquired in 2020–2021. The first flat field was applied to the images before 2019 September 17, and the new flat field was applied to images from 2019 September 17. Both flat fields are publicly available in the calib directory of DARTS data sets.<sup>25</sup> Using star observations between 2010 and 2020, the calibration correction factors ( $\beta$ ) were calculated. The averaged  $\beta$  are  $1.533 \pm 0.208$  at 365 nm and  $1.991 \pm 0.279$  at 283 nm. These  $\beta$  are close to the values reported in Yamazaki et al. (2018). We notice a weak sensitivity change with time at 283 nm, but this is not evident at 365 nm. Star observations by UVI will continue, so we will examine possible sensitivity changes in more detail in the near future. In this study, we took the averaged  $\beta_\lambda$  for each channel ( $\lambda$ ).

We calculated the disk-integrated flux of Venus,  $F_{\text{Venus}}$  in [ $\text{W m}^{-2} \mu\text{m}^{-1}$ ], as follows:

$$F_{\text{Venus}}(\alpha, \lambda, t) = \sum_{r < r_0} \beta_\lambda I(x, y) \times \Omega_{\text{pix}}, \quad (1)$$

where  $\alpha$  is the phase angle,  $\lambda$  is the wavelength,  $t$  is the observation time,  $I$  is the measured radiance at  $(x, y)$  pixel

<sup>25</sup> <https://darts.isas.jaxa.jp/doi/vco/vco-00016.html>

locations on an image,  $\Omega_{\text{pix}}$  is the solid angle of one pixel, and  $r$  is the distance of  $(x, y)$  from the Venus disk center.  $r_o$  is the limiting distance of integration, which includes the Venus radius in pixels and the point-spread function (seven pixels). So  $r < r_o$  defines an area of flux integration from the planet center ( $r = 0$ ) to  $r_o$ . Then, we subtracted the mean background noise per pixel. The solid angle of Venus,  $\Omega_{\text{Venus}}(t)$ , was calculated as

$$\Omega_{\text{Venus}}(t) = \pi \left( \arcsin \left( \frac{R_{\text{Venus}}}{d_{\text{V-obs}}(t)} \right) \right)^2, \quad (2)$$

where  $R_{\text{Venus}}$  is the radius of Venus and  $d_{\text{V-obs}}$  is the distance of the spacecraft from Venus in km at the time of observation  $t$ . For  $R_{\text{Venus}}$ , we considered the cloud-top altitude from the center of the planet (6052 + 70 km).

We calculated the disk-integrated albedo  $A_{\text{disk-int}}$ , as the following (Sromovsky et al. 2001):

$$A_{\text{disk-int}}(\alpha, \lambda, t) = \frac{\pi}{\Omega_{\text{Venus}}(t)} \frac{d_{\text{V-S}}(t)^2 F_{\text{Venus}}(\alpha, \lambda, t)}{S_{\odot}(\lambda)}, \quad (3)$$

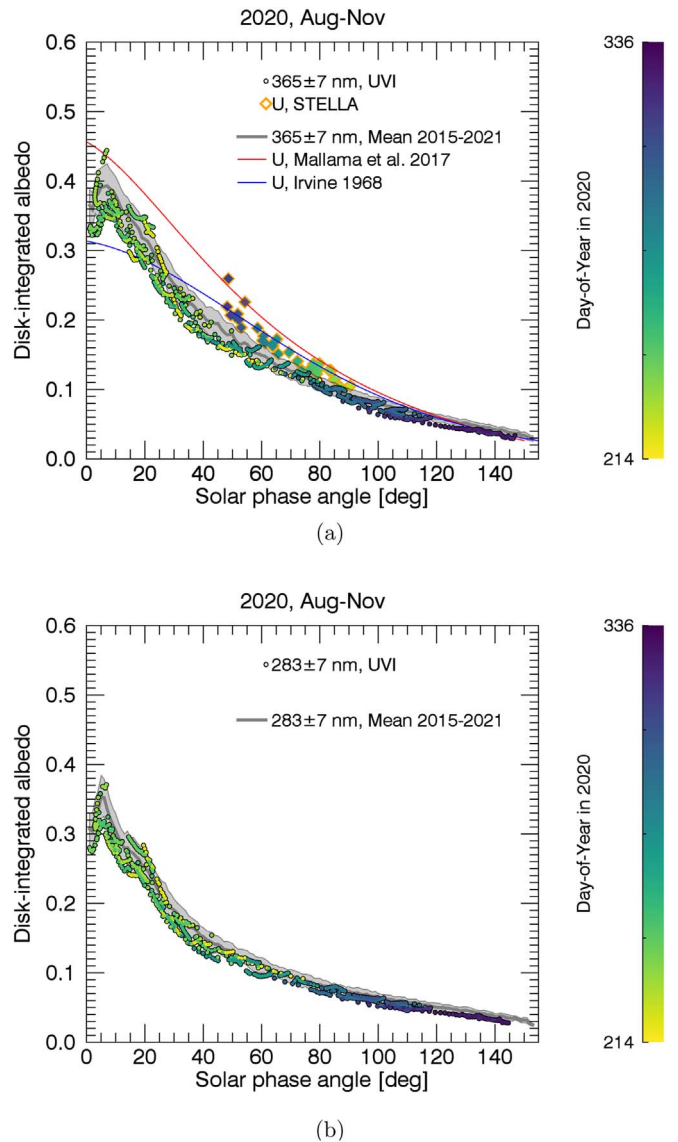
where  $d_{\text{V-S}}(t)$  is the distance between Venus and the Sun [au] at the time of observation  $t$ ,  $\Omega_{\text{Venus}}(t)$  is the solid angle of Venus as viewed from Akatsuki, and  $S_{\odot}(\lambda)$  is the solar irradiance at 1 au [ $\text{W m}^{-2} \mu\text{m}^{-1}$ ] (see Section 3.6), calculated for the transmittance functions of each filter.  $A_{\text{disk-int}}$  is similar in meaning to the radiance factor (Hapke 2012) that can be applied to spatially resolved images.  $A_{\text{disk-int}}(\alpha = 0^\circ, \lambda)$  is the ‘‘geometric albedo’’ at wavelength  $\lambda$ .

Figure 2 shows the mean phase curves at the two channels between 2015 and 2021 (gray lines). The colored circles indicate the data between 2020 August and November, when our ground-based  $U$ -band observations were conducted (see Section 3.4 for details). The symbols show consistent phase angle dependence within the standard deviations of the mean phase curve (the light gray area). The ground-based  $U$  band is wider (34 nm) than the UVI band (14 nm), which may be the reason for the systematic offset. Previously reported mean phase curves for the  $U$  band are compared in the same plot. The Irvine et al. (1968)  $U$  band has the largest bandwidth (116 nm). Mallama et al. (2017) adopted the phase angle dependence of the  $B$  band for the  $U$  band, and adjusted the geometric albedo to match previous observations. Details of these  $U$  bands are provided in Section 3.4.

### 3.2. BepiColombo/PHEBUS

BepiColombo was launched in 2018 October, and is on its way to Mercury (arrival in 2025). BepiColombo is composed of two spacecraft: the Mercury Planetary Orbiter (MPO) and the Mercury Magnetospheric Orbiter. PHEBUS is the UV spectrometer on board MPO. BepiColombo made two Venus flybys in 2020 October and 2021 August, which became opportunities for close-up observations of Venus (Mangano et al. 2021). During the Venus flybys, PHEBUS acquired data over the nightside and limb, because the dayside of Venus was too bright for the PHEBUS sensor, which is designed to detect faint UV emissions from the atmospheric gases of Mercury and the nightside albedo of Mercury (Qu  merais et al. 2020).

The observations of the Venus dayside used here were obtained from a long distance, when the tiny planetary disk



**Figure 2.** Observed disk-integrated albedo at (a) 365 nm and (b) 283 nm as a function of phase angle. The gray solid lines are the mean phase curve of Akatsuki/UVI, and the light gray filled areas are the standard deviations. The circles are the Akatsuki/UVI data and the orange diamonds are the ground-based  $U$ -band data (Section 3.4). The colors of the filled symbols indicate the observation dates, between 2020 August 1 and November 30, as shown in the colorbar. The red curve in panel (a) is taken from Mallama et al. (2017), converted from magnitude to albedo. The blue curve is taken from Irvine et al. (1968), also converted from magnitude to albedo. Their original magnitudes are shown in Figure 4.

entered the slit of PHEBUS. Between 2020 August 28 and September 2, there were such opportunities: the 66'' apparent size of Venus was within the  $2^\circ \times 0.2^\circ$  FOV (Figure 1), and the PHEBUS team made the first Venus faraway observations. 180–181 images were acquired daily over the consecutive six days with the far-UV (FUV; 145–315 nm) and two near-UV (404 and 422 nm) detectors. The data acquisition was done at 4550V for the Microchannel Plate Intensifier, which alters the gain (Chassefi  re et al. 2010). Dark and effective areas are also measured at 4550V in flight.

While Venus was successfully captured by PHEBUS for six consecutive days, we faced three problems. (1) The first problem was the unrealistic fluctuations in photon counts, which varied day to day. These fluctuations were later found to

be caused by the pointing accuracy. The observations aimed to put the disk at the center of the FOV, but the spacecraft's attitude could not put Venus at the center, as planned. Instead, Venus was sometimes located near the boundary of the FOV, according to the later examination, resulting in a significant reduction in the photon counts. This problem prevents the absolute flux analysis, but it should be fine for relative spectral analysis. (2) The second problem was the dark count estimation. The dark measurement (deep space imaging) at 4550V was done a month earlier. As the dark count rate changes with the temperature of the detector, the time difference caused insufficient dark subtraction from the Venus images. The PHEBUS team therefore tried to estimate the dark current, using the photon counts over the deep space pixels outside the Venus illuminating area. We confirmed consistent day-to-day patterns, although this may have introduced additional small errors. (3) The third problem was the effective area retrieval at 4550V, which was determined with the observations of Spica on 2020 February 4. The retrieved effective area was as expected at wavelengths shorter than 270 nm, but at longer wavelengths it turned out to be insufficient for obtaining reliable results. This third problem became critical, as it meant that we could not compare the brightness with the UVI data at 283 nm, and we could not quantify either the relative absorption by the SO<sub>2</sub> gas over the 240–315 nm wavelength range (see Section 6 for details).

After the examination explained above, we excluded the PHEBUS data from the scientific analysis in this paper. Looking into the future, PHEBUS should provide valuable information for retrieving the disk mean SO<sub>2</sub> gas abundance, and to understand the unknown absorber in the FUV spectral range, which are the main goals of the campaign. Future PHEBUS observations will resolve the three problems that we have identified during this campaign.

### 3.3. CAHA1.23/DLR-MKIII

The DLR-MKIII CCD camera installed at the CAHA 1.23 m telescope performed Venus observations in the Johnson–Cousins *BVRI* bands. From August 22 to 28 UTC, Venus was visible right before the sunrise. Venus's apparent diameter changed from 22" to 20" during this period. HR2208 was selected as a solar-like reference star; its spectral type is G2V (Stepien & Geyer 1996)–G5V (Gray et al. 2003), and it was sufficiently bright near Venus, at the same airmass range as Venus. The photometric variability of the star is reported to be 0.03 and 0.035 mag at *V* and *B*, respectively, with a 7.8 day period (Stepien & Geyer 1996). This level of variation has a negligible impact on this study, as our accuracy does not reach such a level; this is comparable to the daily standard deviations of our measurements.

The Venus images were taken under strongly defocused conditions (Gillon et al. 2009; Southworth et al. 2009), to spread photons of Venus over the wide FOV of the CCD camera. This successfully prevented the saturation of the Venus images, without a neutral density filter. This benefits accurate flux measurements of Venus. Star observations were done at the normal focus position. One observation cycle was composed of Venus and the star imaging at the four filters (at least four images per filter per object), and this cycle was repeated three to four times each night.

Usual aperture photometry was used to determine the aperture sizes for integrating the fluxes of Venus and the star,

and we calculated the signal-to-noise ratio (S/N) at the corresponding aperture sizes with the CCD equation. The typical S/N of Venus is  $\sim 10^5$  and that of the star is 1000–2000. Atmospheric extinction coefficients were determined at each filter, by using a linear regression between the instrumental magnitude of the star and the airmass. The airmass ranges were 1.6–2.1 each night for both Venus and the star. The atmospheric extinction coefficients were consistent for the first five nights. During the last two nights, partial clouds entered the view, resulting in temporally variable telluric opacity. Since the instrumental magnitude at zero airmass is known to be stable for the CAHA1.23 DLR-MKIII camera, we could also compute the instantaneous extinction coefficient at the time of the Venus observations by interpolation during nonphotometric nights, thanks to the repeated cycles between Venus and the star. The apparent magnitude of Venus was calculated with the interpolated atmospheric extinction coefficient and the known magnitudes of the star (Table 2).

The apparent magnitude of Venus was converted to the reduced magnitude, which is the brightness at 1 au from both the Sun and the Earth. The distances between the Sun and Venus, and the Earth and Venus, at the time of imaging were calculated using the JPL SPICE toolkit (Acton 1996). Hereafter, magnitude refers to the reduced magnitude, and the results are shown in Figure 3. The comparison with the brightness reported by Mallama et al. (2017) shows a good agreement with the expected brightness at  $\alpha \sim 80^\circ$  at the four bands (for the daily variation, see Figure 8).

### 3.4. STELLA/WiFSIP

The WiFSIP wide-field imager installed at the STELLA 1.2 m robotic telescope conducted Venus imaging at the *U* band. The period of observations continued between 2020 August 11 and November 8, except the time when a Sahara dust storm affected the telescope's site in Tenerife. The observations were conducted before sunrise every day. For about 30 minutes, a bright solar-like reference star near Venus was continuously observed to define the telluric extinction coefficient. Then the Venus imaging followed immediately, when Venus rose high in the dark sky. Typically, 15 Venus images were acquired each night (except August 12, when five images were acquired). The airmass of Venus changed with the time of the observations: 1.6–1.7 from August 11 to September 14, 1.7–1.8 from September 20 to October 2, 1.8–2.0 from October 3 to 27, and 2.0–2.4 until November 8.

Aperture photometry was applied to determine the size of the area for integrating the Venus flux and reference stars. The typical S/N of Venus is 6000–8000, and those of stars range from  $\sim 500$  to  $\sim 3000$ , depending on the stars. Following the locations of Venus on the sky, our reference stars changed with time (Table 2). Note that  $\kappa$  Gemini has an accompanying star, and its corresponding pixels were excluded from the aperture photometry. The ranges of star airmass varied with time, e.g., 1.9–2.2 on August 11, 1.4–1.9 on September 14, 1.5–2.0 on October 10, and 1.6–1.75 on November 8. Daily extinction coefficients were monitored, and we excluded dates of abnormal behavior compared to the other dates. Our averaged extinction coefficient for the *U* band is  $0.485 \pm 0.093$ . The apparent magnitude of Venus was calculated with the daily atmospheric extinction coefficient and the known magnitudes of each star (Table 2). The apparent magnitude was converted to the reduced magnitude, as described in Section 3.3.

**Table 2**  
Reference Stars for Imaging Observations

Star	Spectral Type	Magnitude					Reference of Magnitude	Dates of Observation
		<i>U</i>	<i>B</i>	<i>V</i>	<i>R</i>	<i>I</i>		
(1)	(2)	(3)	(4)	(5)	(6)	(7)	(8)	(9)
HR2208	G2V–G5V	7.317	7.131	6.456	6.087	5.740	Stepien & Geyer (1996)	Aug 11–Sep 4
$\kappa$ Gemini	G8III–IIIb	5.19	4.49	3.57	2.86	2.41	Ducati (2002)	Sep 6–13
$\mu$ .02 Cnc	G1IVb	6.14	5.93	5.30			Ducati (2002)	Sep 14–30
35 Leo	G1.5IV–V	6.85	6.64				Ducati (2002)	Oct 2–10
HD88725	G3/5V	8.34	8.33	7.73	7.24	6.89	Ducati (2002)	Oct 14–24
HD92719	G1.5V	7.519	7.406	6.767	6.42	6.083	Koen et al. (2010)	Oct 27–Nov 8

Our STELLA *U*-band magnitude measurements are, to the best of our knowledge, the first after Irvine et al. (1968). The comparison of these data sets is shown in Figure 4. As a reference, two more data sets are shown together: the oldest measurement (Knuckles et al. 1961) and a recent estimation (Mallama et al. 2017). The comparison of our data with Irvine et al. (1968) shows a consistent magnitude, but it is in fact an inadequate comparison, considering the larger bandwidth of Irvine et al. (1968; 116 nm) than of STELLA (34 nm). Mallama et al. (2017) estimated the *U*-band phase curve that follows the phase angle dependence in the *B* band and has the geometric albedo, to be consistent with the two older *U*-band observations. Knuckles et al. (1961) show a much brighter Venus magnitude, and it is difficult to understand the cause of such a difference. In this study, we have adopted the Irvine et al. (1968) phase curve as a reference phase curve at *U* to correct the phase angle dependence of the STELLA data (Equation (8) in Section 5).

The fluctuation of STELLA’s *U* band is noticeable in Figure 4. These may be real short-term fluctuations, as reported in a recent study of Venus’s disk-integrated albedo (Lee et al. 2020; see Section 5.1). The Venus monitoring by STELLA will continue, and we should be able to construct the true mean phase curve at *U* and extract accurate temporal variations in the near future.

### 3.5. CAHA3.5/PMAS

PMAS is installed at the CAHA 3.5 m telescope (Roth et al. 2005), and it acquired Venus data from 2020 August 26 to 29. The Venus observations were conducted with the bare fiber bundle integral field unit (PPAK), which has a wide hexagonal FOV of  $65'' \times 74''$ , as shown in Figure 5(a). A total of 331 fibers obtained scientific data within the FOV, and an additional 36 fibers simultaneously acquired sky data at  $72''$  away from the center of the FOV. The wide FOV is sufficient for capturing the entire Venus disk, which had an apparent diameter of  $\sim 20''$ .

PMAS is optimized to observe faint objects. In fact, Venus is too bright for PMAS in its normal operation mode, so the Venus observation was conducted with special care; only one petal of the mirror cover was open, to reduce the photon flux. Our targeted spectral range of the observation, from UV to blue color, also helped to reduce the photon flux of Venus due to telluric extinction. We acquired high-spectral resolution data,  $d\lambda = 0.28$  nm, which effectively spread the photons between 326.1 and 478.3 nm, using the U1200 grating.

The Venus data were acquired at the end of each night, for about an hour, with a 0.4 s exposure time, resulting in  $\sim 100$  images per night. The airmass of Venus ranged typically

between 1.5 and 2.5 each night, and only the data with airmass close to that of our reference star observations were selected for the analysis. Reference star observations were conducted at the beginning of night, in the middle, and right before the Venus observations. 10Lac, Vega, and eps Aqr were observed each night, and we eventually used 10Lac (CALSPEC database;<sup>26</sup> Bohlin et al. 2014) to construct the telluric transmittance function, which makes use of PMAS’s high spectral resolution. Two sets of 10Lac observations were conducted each night, between 1.3 and 1.7 airmass.

The P3D version 2.7 package was used for the data reduction (Sandin et al. 2010), which includes creating a master bias image, tracing spectra, finding spectral positions, and generating a flat field, and ultimately produces a reduced spectral image. We integrated the flux of the targets as follows (Rosales-Ortega et al. 2010). We subtracted the median sky spectrum from the scientific data in each image. From the center of Venus or the reference star (e.g., the black “X” in Figure 5(a)), we increased the area of flux summation, until the total flux did not increase further ( $< 1\%$ ) over the entire wavelength range. Such radii were  $16''$  for Venus and  $12''$  for 10Lac. The selected fibers of the flux integration area are marked with white circles in Figure 5(a), and the total flux spectrum of Venus is shown in Figure 5(b).

We generated a reference telluric transmittance function  $T_{\text{ref}}(\lambda)$  each night (Wytttenbach et al. 2015), as

$$T_{\text{ref}}(\lambda) = \exp(E_{\lambda} s_{\text{ref}}), \quad (4)$$

where  $\lambda$  is the wavelength,  $E_{\lambda}$  is the telluric optical depth at zenith, and  $s_{\text{ref}}$  is the mean airmass of the reference star observations. The difference from Wytttenbach et al. (2015) is that the transmittance is not at the unity airmass (zenith), but at  $s_{\text{ref}}$ .

We calculated  $E_{\lambda} s_{\text{ref}}$  as follows. The logarithm of the measured star fluxes  $F_{\text{obs,star}}(\lambda)$  has a linear relationship with the airmass  $s$  (Langeveld et al. 2021), as

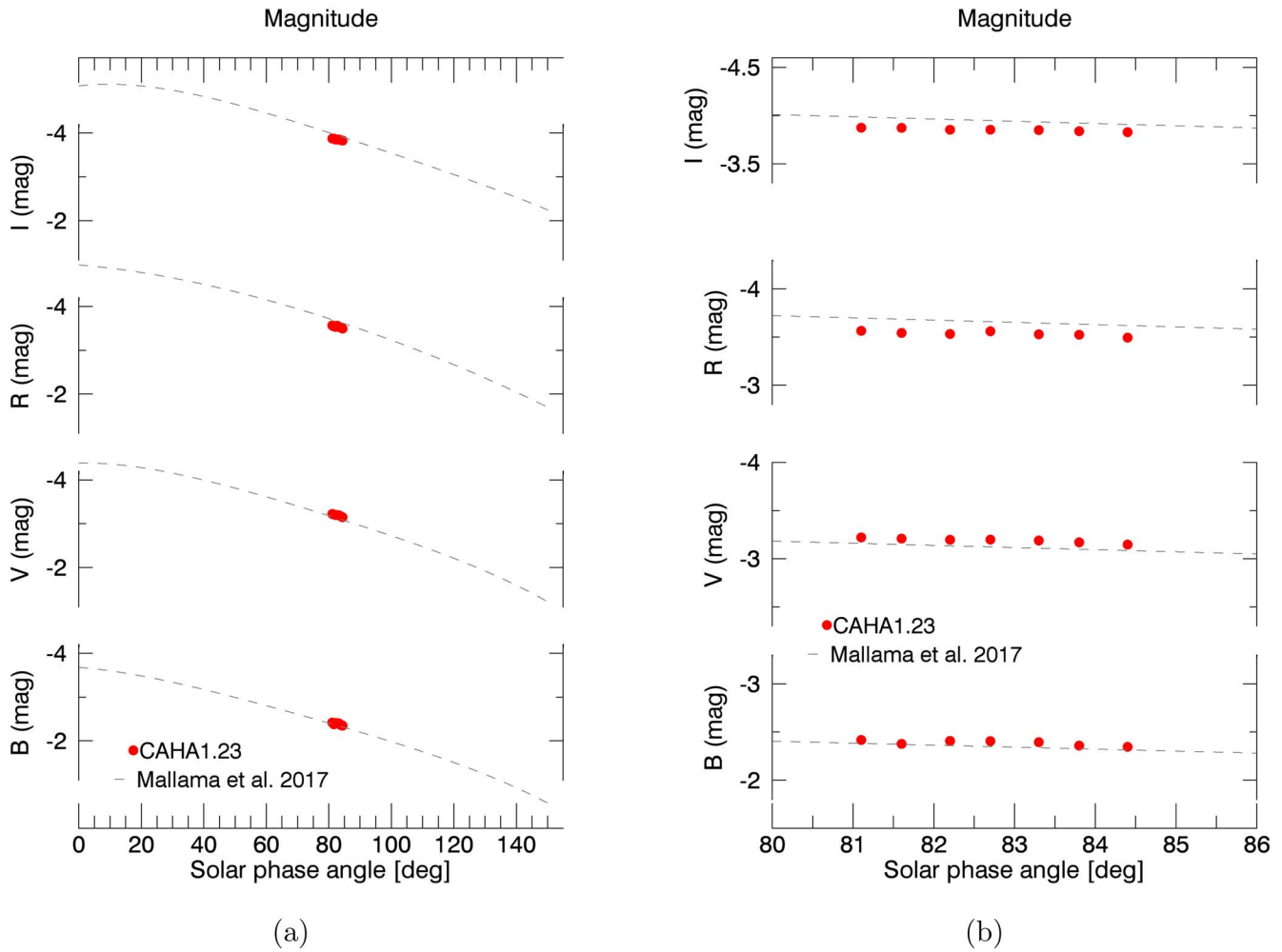
$$\ln(F_{\text{obs,star}}(\lambda)) = E_{\lambda} s + c, \quad (5)$$

where  $c$  is a constant. As the standard star flux spectrum  $F_{\text{std}}(\lambda)$  is at  $s = 0$ , we can convert the equation above as

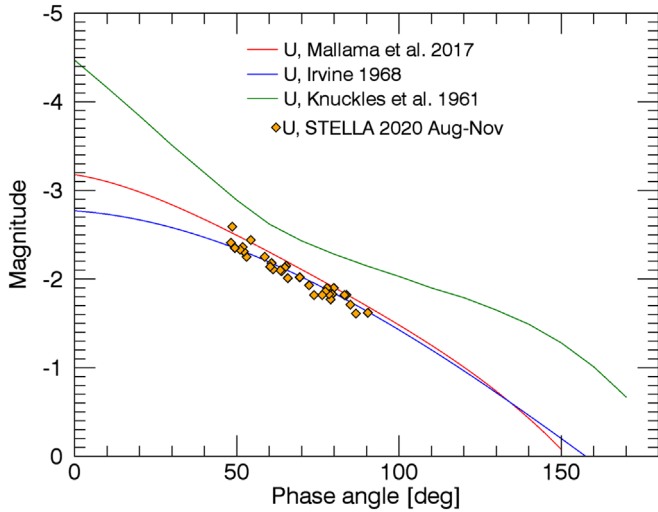
$$\ln(F_{\text{obs,star}}(\lambda)) - \ln(F_{\text{std}}(\lambda)) = E_{\lambda} s + c_0, \quad (6)$$

where  $c_0$  is a constant that makes the result zero at 445 nm, which is the center of the Johnson *B* band. We normalized the transmittance functions to those at 445 nm, and averaged two

<sup>26</sup> [https://archive.stsci.edu/hlsps/reference-atlases/cdbs/current\\_calspec/10lac\\_mod\\_003.fits](https://archive.stsci.edu/hlsps/reference-atlases/cdbs/current_calspec/10lac_mod_003.fits)



**Figure 3.** Observed magnitudes of Venus in the Johnson–Cousins *BVRI* bands between 2020 August 22 and 28 by the CAHA1.23/DLR-MKIII camera (red dots). (a) Phase curves over the range from  $0^\circ$  to  $150^\circ$ . (b) The same as (a), but close-up representations of the observed data points of the campaign. The phase curves at each band are shown with the gray dashed lines (Mallama et al. 2017).



**Figure 4.** Observed magnitude of Venus in the Johnson *U* band by STELLA/WiFSIP in 2020 August–November (orange diamonds). The phase curves reported in previous studies are compared: Knuckles et al. (1961; green), Irvine et al. (1968; blue), and Mallama et al. (2017; red).

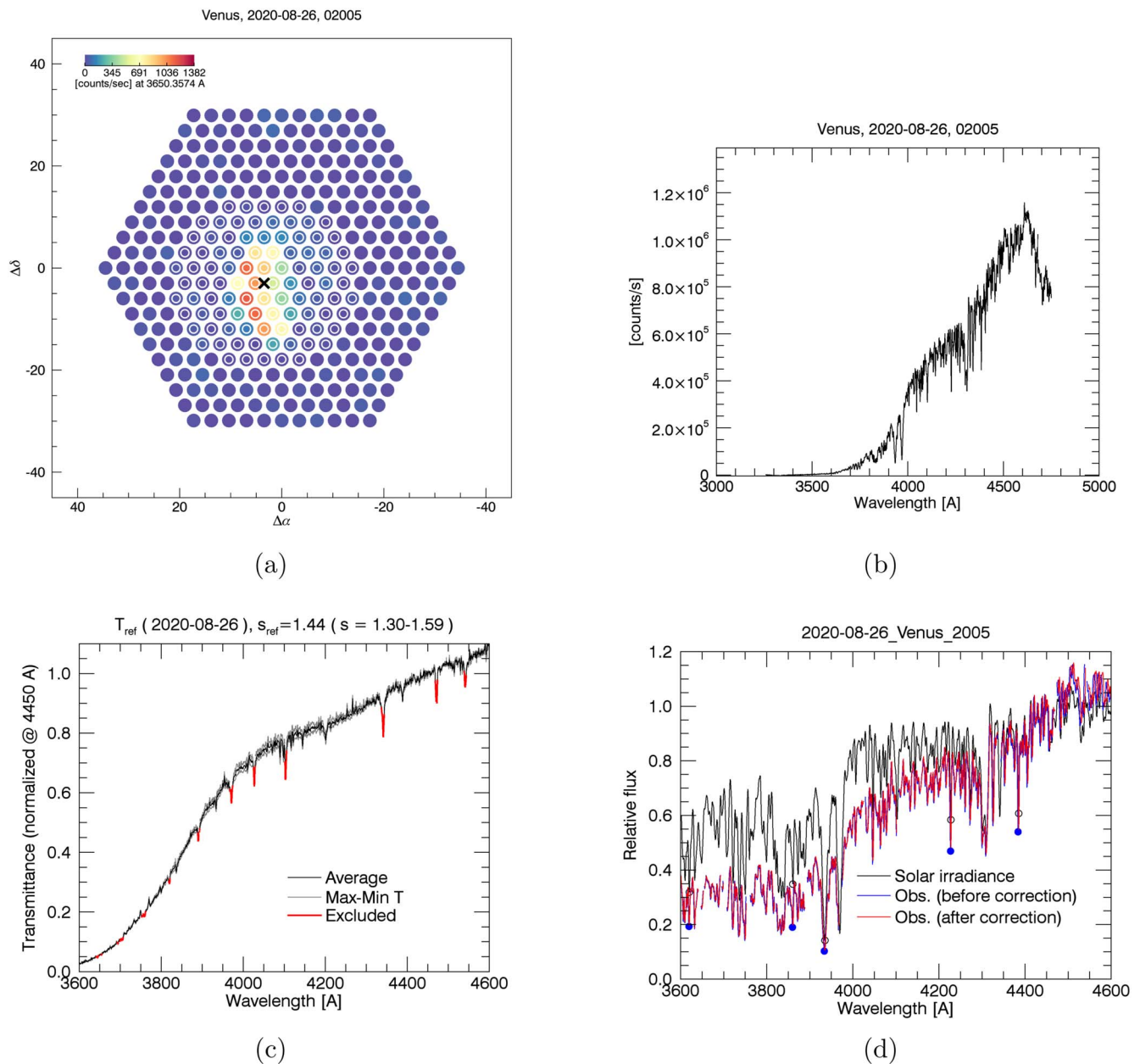
sets of normalized transmittance functions. The  $T_{\text{ref}}(\lambda)$  on August 26 is shown in Figure 5(c) (black curve). Fine emission lines of the star are excluded from this process (red intervals).

We retrieved relative flux spectra of Venus  $F_{\text{Venus}}(\lambda)$  using  $T_{\text{ref}}(\lambda)$ ; after selecting the observed Venus fluxes  $F_{\text{obs,venus}}(\lambda)$  that were acquired at  $s$  near the star observations ( $ds < 0.1$ ) each night, we divided these Venus fluxes by  $T_{\text{ref}}(\lambda)$  of the same night:

$$F_{\text{Venus}}(\lambda) = \frac{F_{\text{obs,venus}}(\lambda)}{T_{\text{ref}}(\lambda)}. \quad (7)$$

An example of the relative Venus flux spectrum on August 26 is shown in Figure 5(d) (the blue curve, which almost overlaps with the red curve). A comparison between the Venus flux and the solar irradiance (Section 3.6) is shown in the same figure. Using the selected spectral features of the solar reference (the circle symbols), we slightly adjusted the spectral location of the Venus spectrum, as shown in the same plot, before (blue) and after (red) the adjustment. Such spectral location adjustments were done between  $-4$  and  $+3 \text{ \AA}$ , depending on the dates of the observations and the wavelengths. This last process shows only minor changes, but helps to remove unrealistic humps from the reflectivity spectrum. We repeated the same procedure for the data of each night, to generate daily mean Venus spectra.





**Figure 5.** PMAS observation and calibration examples of the data acquired on 2020 August 26 (image number 2005). (a) An image slice from PPAK at 365 nm after sky subtraction. The strong signals show where the Venus dayside is located. The mean of the strong signal locations is marked with the black “X,” from which a  $16''$  radius circular area is selected for flux integration (the white “o” symbols). (b) Integrated flux spectrum of Venus before the telluric extinction correction. (c) Relative telluric transmittance function  $T_{\text{ref}}(\lambda)$  of the same night (see the text for the details). The star (10Lac) was observed at the airmass  $s$  of 1.30 and 1.59 (gray curves). The mean transmittance is used to define  $T_{\text{ref}}(\lambda)$  (black), except fine emissions of the star (red ranges). (d) Relative flux spectrum of Venus  $F_{\text{Venus}}(\lambda)$ , after the telluric extinction correction (blue). Relative solar irradiance is shown (black). Some features are selected (black circles) as spectral references to adjust the spectral locations of the Venus flux (blue disks). After this fine spectral location correction, the final Venus spectrum is shown as the red curve, which almost overlaps with the blue curve.

### 3.6. Solar Irradiance Data

We converted the observation data to reflectivity using the reference solar irradiance spectrum. We used the observed solar irradiance data from TSIS-1 SIM (Version 6, Level 3, daily data)<sup>27</sup> over the 200–2400 nm wavelength range. For the campaign data of this paper, we averaged the TSIS-1 SIM data from 2020 August to September. This mean solar spectrum was used to calculate the solar irradiance at 283 and 365 nm for the Akatsuki data. We calculated the solar magnitude in the  $U$  band

using the effective transmittance function of STELLA, following the description in Willmer (2018) to take into account its small bandwidth (FWHM = 34 nm). For the  $BVR/I$  broad bands, we took the values given in Willmer (2018). The solar magnitudes in each band are listed in Table 3. For the high-resolution spectral grids of the PMAS data, the TSIS-1 SIM data were not sufficient (5 nm at  $\lambda \sim 400$  nm),<sup>28</sup> so we took the SAO2010 solar reference spectrum, whose spectral resolution is 0.04 nm (FWHM; Chance & Kurucz 2010). We

<sup>27</sup> <https://lasp.colorado.edu/home/tsis/data/>

<sup>28</sup> <https://lasp.colorado.edu/home/tsis/instruments/sim-spectral-irradiance-monitor/>

**Table 3**  
Solar Magnitude

<i>U</i>	<i>B</i>	<i>V</i>	<i>R</i>	<i>I</i>
-26.0	-26.13	-26.76	-27.15	-27.47

convolved the SAO2010 spectrum into the spectral grids of the PMAS data with a Gaussian function, which is shown in Figure 5(d).

#### 4. Atmospheric Structure and Model Calculations

We performed radiative-transfer model calculations to compare with the observed reflectivity of Venus. The atmospheric structure and the model configurations are described in this section.

##### 4.1. Atmospheric Gases

We took into account the atmospheric gaseous absorption of CO<sub>2</sub>, SO<sub>2</sub>, OCS, O<sub>3</sub>, SO, H<sub>2</sub>O, H<sub>2</sub>S, HCl, HF, and CO. We also considered CH<sub>4</sub>, which was tentatively detected by the Pioneer Venus Large Probe Neutral Mass Spectrometer (Donahue & Hodges 1993), although this detection is questionable, as stated by the authors. Subsequently, CH<sub>4</sub> was excluded from our analysis (Section 5), due to its too strong absorption signature in the near-infrared (NIR; Appendix), which cannot be missed in spectral observations—for example, the spectrum of MESSENGER/MASCS, as shown in Pérez-Hoyos et al. (2018). A similar conclusion is also drawn from a nightside spectral data analysis at the 2.3 μm atmospheric window, providing the upper limit of methane as <0.1 ppm at 30 km altitude (Pollack et al. 1993). The detection of CH<sub>4</sub> may require future observations to confirm its possible presence (Johnson & de Oliveira 2019; Bains et al. 2021), and this is beyond the concern of this study.

Altitudes between 48 and 100 km were modeled in this study, including the sulfuric acid cloud layer (Section 4.2). Molecular number density was calculated as a function of altitude using the atmospheric temperature and pressure profiles at low latitudes (Seiff et al. 1985). Gaseous absorption has been calculated as a function of either temperature (especially for the UV absorption cross sections) or altitude, which considers both the temperature and pressure of Venus (for the line-by-line calculations).

We compared the available cross-sectional data sets in the UV–visible wavelength range of SO<sub>2</sub>, OCS, O<sub>3</sub>, CO<sub>2</sub>, SO, H<sub>2</sub>O, H<sub>2</sub>S, and HCl, and finally selected those shown in Table 4. We selected data that were published in recent years and measured experimentally, or recommended by another database, such as the JPL compilation by Burkholder et al. (2019). SO<sub>2</sub>, OCS, and CO<sub>2</sub> absorption is known to depend on temperature. We assumed linear functions of temperature for the cross sections of SO<sub>2</sub> (Vandaele et al. 2009) and OCS (Grosch et al. 2015). That of CO<sub>2</sub> was calculated with exponential functions, following Hartinger et al. (2000) and Venot et al. (2018).

At the longer wavelengths, from the visible to the NIR wavelength, we calculated line-by-line cross sections with a 0.1 cm<sup>-1</sup> spectral resolution, using Huang et al. (2017) for CO<sub>2</sub> and HITRAN2016 (Gordon et al. 2017) for H<sub>2</sub>O, H<sub>2</sub>S, HCl, HF, and CO. The sub-Lorentzian factor of the CO<sub>2</sub> absorption was assumed to be that of the CO<sub>2</sub> atmospheric windows

between 1.18 and 2.3 μm, which produced a reasonable fit with the observations (Meadows & Crisp 1996). We used a 300 cm<sup>-1</sup> line cutoff value, which is longer than the 200 cm<sup>-1</sup> used in a previous study (Lee et al. 2016), instead of assuming a possible CO<sub>2</sub> continuum. All other gases used a 100 cm<sup>-1</sup> line cutoff value without the assumption of a sub-Lorentzian factor. Rayleigh scattering was calculated for the atmosphere, composed of 96.5% CO<sub>2</sub> and 3.5% N<sub>2</sub>, with cross sections by Snee & Ubachs (2005). A summary of the gaseous absorption cross-sectional data at room temperature is shown in Figure 6(a). The cross section of the Rayleigh scattering is also plotted for comparison. Figure 6(b) shows the extinction coefficients of gases at the cloud-top atmosphere (~70 km), with the assumed abundances of the trace gases (Figure 6(c)). In Figure 6(b), the dominant CO<sub>2</sub> absorption is noticeable at the short-wavelength edge, while Rayleigh scattering dominates over the other wavelengths. We note that the SO<sub>2</sub> and O<sub>3</sub> absorption bands overlap around 250 nm. We also note that the SO, SO<sub>2</sub>, and H<sub>2</sub>S absorption overlap at λ < 240 nm. H<sub>2</sub>S, if its presence is confirmed, may cause a complication in retrieving the abundance of the SO gas in low-spectral resolution data, and this was not considered in a previous study (Belyaev et al. 2012).

The vertical profiles of gaseous abundance (Figure 6(c)) were assumed as follows. CO<sub>2</sub> was fixed to 96.5% (Seiff et al. 1985). A recent observation analysis revealed the cloud-top level O<sub>3</sub> (Marcq et al. 2019), and its global mean value was assumed as ~1 ppbv at 55–70 km altitude. Chemistry model calculations suggested the possible presence of H<sub>2</sub>S (Bierson & Zhang 2020), and their nominal model profile was adopted in this study: ~10 ppbv near 70 km altitude, and decreasing above. This abundance of H<sub>2</sub>S is lower than that used in a previous study (Titov et al. 2007), whose atmospheric model was based on in situ measurements at lower altitudes (≤55 km; von Zahn & Moroz 1985). The observed SO<sub>2</sub> and SO abundances at the cloud-top level are highly variable (Encrenaz et al. 2019; Marcq et al. 2020); we assumed the SO<sub>2</sub> abundance at 70 km to be 22.4 ppbv (Lee et al. 2021) and SO to be 10% of SO<sub>2</sub>, following Marcq et al. (2020). The vertical distribution of the SO<sub>2</sub> gas abundance was assumed to change with a scale height of 3 km (Marcq et al. 2020). We also assumed HCl to be 0.6 ppmv (Connes et al. 1967), and followed the assumptions in Titov et al. (2007) for OCS, H<sub>2</sub>O, HF, and CO. While testing the impact of CH<sub>4</sub> on the simulated spectrum, 980 ppmv was assumed (Donahue & Hodges 1993; Appendix).

##### 4.2. Clouds

Two different sizes of cloud aerosols were taken into account in this study, the so-called “mode 1 and 2”: mode 1 with  $r_{\text{eff}} = 0.43 \mu\text{m}$  and  $\nu_{\text{eff}} = 0.52$  (Pollack et al. 1980), and mode 2 with  $r_{\text{eff}} = 1.26 \mu\text{m}$  and  $\nu_{\text{eff}} = 0.076$  (Lee et al. 2017) (Table 5). The spectral dependences of the optical properties of the aerosols were calculated with the log-normal size distribution, using a Lorentz–Mie code (Mishchenko et al. 2002). The refractive indices of the aerosols were taken from Hummel et al. (1988) for 75% H<sub>2</sub>SO<sub>4</sub>–H<sub>2</sub>O aerosols. As shown in Figure 7(a), the extinction coefficient of the aerosols shows little change over the spectral range of this study. The asymmetry factor ( $g$ ) shows spectral variation (Figure 7(b)). We prescribed the relative abundances of modes 1 and 2 by imposing the ratio of extinction between the two modes of aerosols as 1:1 at 365 nm. This extinction ratio is similar to the

**Table 4**  
Gaseous Absorption Data Set

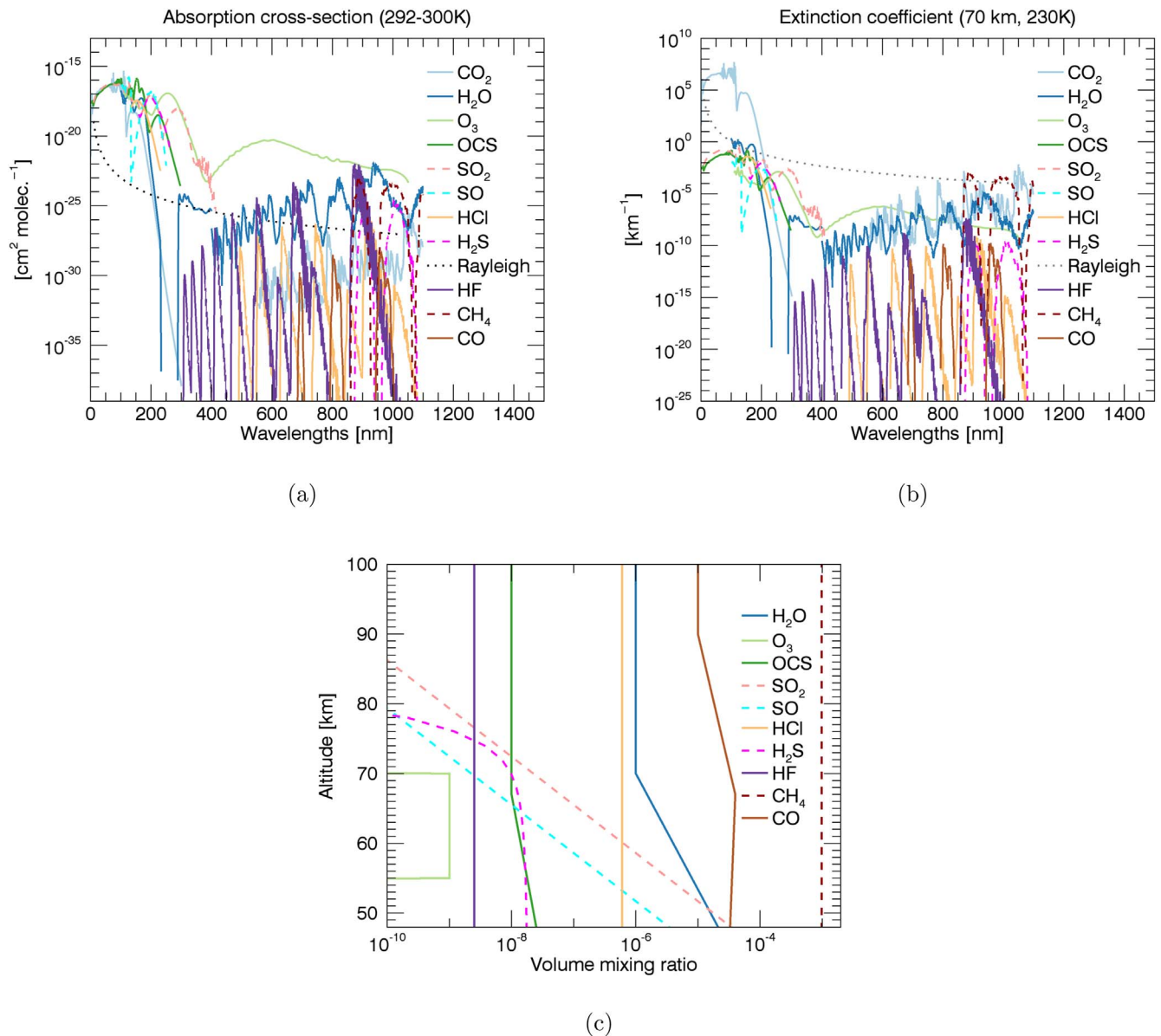
Gas	Wavelength (nm)	Measured Temp. (K)	Dependence		Reference (Data Source, if Applicable)
			Temp. (4)	Pres. (5)	
(1)	(2)	(3)	(4)	(5)	(6)
SO <sub>2</sub>	10–106	298	×	×	Feng et al. (1999) (MPI-Mainz Atlas <sup>1</sup> )
	106–230	293	×	×	Manatt & Lane (1993) (MPI-Mainz Atlas)
	230–417	298–358	o(linear)	×	Vandaele et al. (2009); Hermans et al. (2009)
OCS	3.44–115	298	×	×	Feng et al. (2000a, 2000b) (Heays et al. 2017)
	115–190	298	×	×	Limão-Vieira et al. (2015) (Heays et al. 2017)
	190–205	295	×	×	Molina et al. (1981) (JPL recommendation 2000 <sup>2</sup> , MPI-Mainz Atlas)
	≤315	294.8–773.2	o(linear)	×	Grosch et al. (2015) (MPI-Mainz Atlas)
O <sub>3</sub>	110–195	298	×	×	Mason et al. (1996)
	197–825	293–298	×	×	(JPL recommendation 2000)
	853–1047	294	×	×	Table 8 in Helou et al. (2005)
CO <sub>2</sub>	0.125 4–106.15	300	×	×	Huestis & Berkowitz (2011)
	106.15–115	195, 295	o <sup>3</sup>	×	Stark et al. (2007)
	115–230	150–800	o	×	Venot et al. (2018)
	556–1000	...	o	o	Huang et al. (2017)
SO	190–220	293	×	×	Phillips (1981)
	190, 220	...	×	×	Gaussian fit of Phillips (1981) <sup>4</sup>
H <sub>2</sub> O	99.9–114	298	×	×	Fillion et al. (2004) (MPI-Mainz Atlas)
	114–140	298	×	×	Mota et al. (2005) (MPI-Mainz Atlas)
	140–190	298	×	×	(JPL recommendation 2000)
	192–230	292	×	×	The extrapolated model of Ranjan et al. (2020) (MPI-Mainz Atlas)
	290–325	295	×	×	Table 1 in Pei et al. (2019)
	325–400	293	×	×	The upper limits of Wilson et al. (2016) (MPI-Mainz Atlas)
	400–1000	...	o	o	(HITRAN2016 <sup>5</sup> )
H <sub>2</sub> S	160–260	170–370	o	×	Wu & Chen (1998) (MPI-Mainz Atlas)
	833–1000	...	o	o	(HITRAN2016)
HCl	135–230	298	×	×	Bahou et al. (2001)
	476–1000	...	o	o	(HITRAN2016)
HF	303–1000	...	o	o	(HITRAN2016)
CO	667–1000	...	o	o	(HITRAN2016)
CH <sub>4</sub>	833–1000	...	o	o	(HITRAN2016)

**Notes.** <sup>1</sup> Keller-Rudek et al. (2013). <sup>2</sup> Burkholder et al. (2019). <sup>3</sup> Hartinger et al. (2000). <sup>4</sup> The Gaussian fit of the SO absorption cross section,  $\sigma(\lambda) [\text{cm}^2] = A_0 \exp\left(-\frac{(\lambda - A_1)^2}{2 \times (A_2)^2}\right)$ , where  $\lambda$  is the wavelength in [nm],  $A_0 = 1.15633 \times 10^{-17} \text{ cm}^2$ ,  $A_1 = 194.665 \text{ nm}$ , and  $A_2 = 11.2838 \text{ nm}$ . <sup>5</sup> Gordon et al. (2017).

ratio in the upper cloud layer inferred from the Pioneer Venus Sounder Probe (Knollenberg & Hunten 1980; Pollack et al. 1980). Our initial cloud-top altitude was assumed to be 70 km at 365 nm, changing vertically by a scale height of 4 km, close to the value retrieved previously (Ignatiev et al. 2009; Lee et al. 2012; Satoh et al. 2015). The cloud-top altitude ( $\tau = 1$ ) shows little change over the entire wavelength range of this study (Figure 6(c)). We later change this cloud-top altitude to 64 km in Section 5, to fit our observed *I*-band reflectivity. This cloud-top altitude is still tentative, and we plan further studies to examine reliable cloud-top altitude retrieval using ground-based observations.

At first, we simulated the reflectivity of Venus without the unknown absorber, which could not fit the observed reflectivity (Section 5.2). Later, we took into account the unknown absorber in explaining the observations (Section 5.3). We assumed that the unknown absorber is present in a 6 km thick layer, whose middle altitude is located 3 km below the cloud-top level, which was one of the best solutions in our previous

study (Lee et al. 2021). To simulate the unknown absorber, we reduced the single scattering albedo (SSA) of the cloud aerosols within the 6 km layer, by increasing the absorption relative to the extinction coefficient strictly attributable to the aerosols ( $R_{\text{UA}}$ ):  $\text{SSA} = 1 - R_{\text{UA}}$  (Lee et al. 2021). This parameterization imitates the impact of a variable imaginary refractive index ( $n_i$ ) of the cloud aerosols at our target wavelengths, since the SSA is the factor that is most sensitive to variable  $n_i$  among all the optical properties of the cloud aerosols, such as the extinction cross section and  $g$ . This simplified approach helps us to quantify the influence of the unknown absorber, even though we do not know its identity—for example, which size of aerosols would contain the absorber, or whether the absorber is solid or gaseous. In this study, we reduced the SSA of both mode 1 and mode 2 aerosols to account for the contribution of the unknown absorber. This assumption keeps the model configuration simple, and is consistent with the fact that all modes may contain the absorber as an impurity in particles (Pollack et al. 1980).



**Figure 6.** Atmospheric gases. (a) Absorption cross sections of the gases considered in this study at room temperature. Rayleigh scattering is also plotted for comparison (dotted line). The dashed lines indicate gases that require careful consideration, due to their highly variable abundances ( $\text{SO}_2$  and  $\text{SO}$ ) or limited observations ( $\text{H}_2\text{S}$  and  $\text{CH}_4$ ). (b) Extinction coefficients of gases at the 70 km altitude atmosphere (near the cloud-top level). (c) Vertical profiles of the gaseous abundances assumed in this study.

**Table 5**  
Size Distributions of the Cloud Aerosols

Mode	$r_{\text{eff}}$ ( $\mu\text{m}$ )	$\nu_{\text{eff}}$	Log-normal Size Distribution	
			$\bar{r}$ ( $\mu\text{m}$ )	$\sigma$
mode 1	0.43	0.52	0.15	1.91
mode 2	1.26	0.076	1.05	1.31

### 4.3. Radiative-transfer Model Calculations

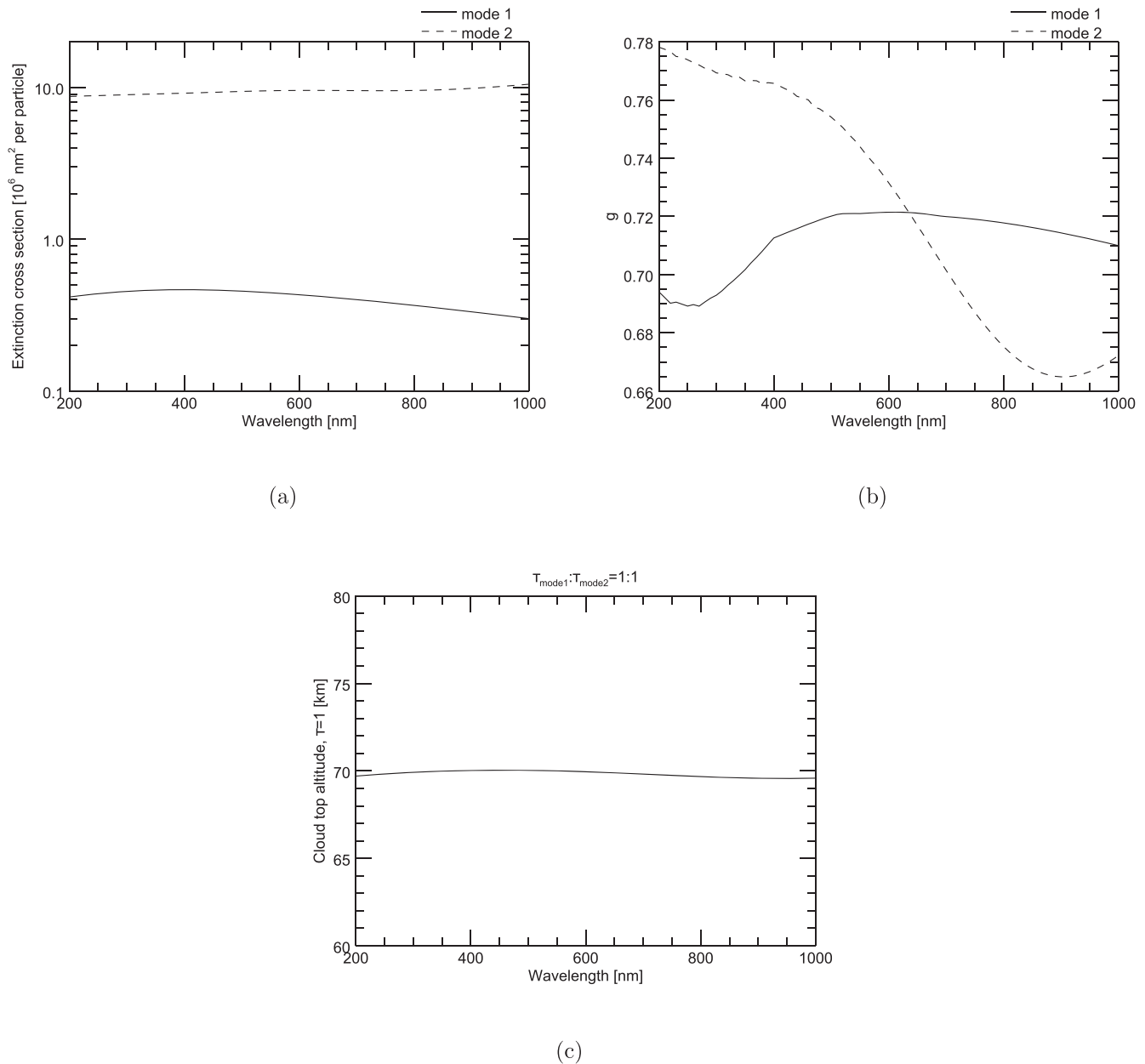
We used a Preconditioned Backward Monte Carlo (PBMC) algorithm (García Muñoz 2015; García Muñoz & Mills 2015) to fit the observed spectral reflectivity of the Venus disk during the campaign period. The solar phase angle ( $\alpha$ ) was fixed to  $80^\circ$ , and we calculated multiple scattering processes in the atmosphere over the 180–1000 nm spectral range. We selected

$d\lambda = 1$  nm, which balances spectral resolution against computing efficiency. At each wavelength grid, we used  $10^6$  photons. The statistic error is 0.05% over the spectral range. The gaseous absorption data set described in Section 4.1 was convolved using a Gaussian function (FWHM = 1 nm), to take into account fine absorption features (Figures 6(a) and (b)). We confirmed that two results are consistent: one with the current configuration, and another that ran PBMC calculations at higher spectral resolution (0.005 nm), then convolved into the 1 nm grid.

## 5. Results

### 5.1. Temporal Variation of the Reflectivity

While the ground-based observations were mostly taken at  $\alpha \sim 80^\circ$  over the morning side (Figure 1(b)), Akatsuki's viewing geometry changed along its orbit: between August 15 and



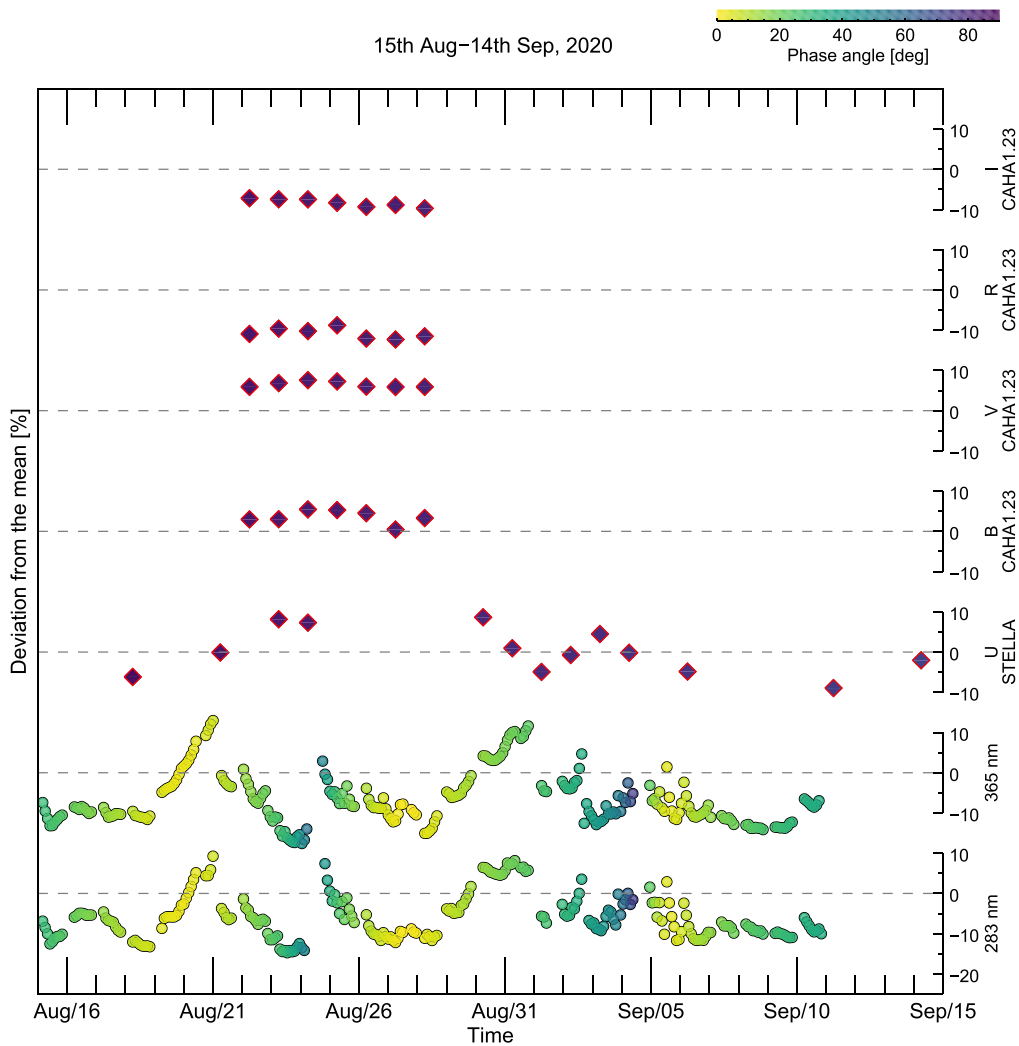
**Figure 7.** Spectral dependences of the optical properties of the clouds. (a) Extinction cross section. (b) Asymmetry factor,  $g$ . (c) Cloud-top altitude (unity tau).

September 15,  $\alpha$  varied from  $0^\circ$  (the full Moon shape) to  $74^\circ$  (the afternoon side). To compare data taken from different viewing geometries, we calculated the relative brightness [%], indicating how far the data at a specific time deviate from the reference phase curve  $A_{\text{disk-int}}$  at the same phase angle (observed mean phase curves or a reference phase curve, such as in Irvine et al. (1968) and Mallama et al. (2017), as explained in Sections 3.1, 3.3, and 3.4):

$$\frac{(A_{\text{disk-int}}(\alpha, t) - \overline{A_{\text{disk-int}}(\alpha)})}{\overline{A_{\text{disk-int}}(\alpha)}} \times 100. \quad (8)$$

The spatial distribution and absolute abundance of the unknown absorber are known to be variable over time (Esposito 1980; Del Genio & Rossow 1990; Markiewicz et al. 2007; Titov et al. 2012; Lee et al. 2019, 2020), and this is also shown in Figure 8, over a period of one month. The

variation range of the relative brightness at 365 nm reaches over 20% (peak to peak). That at 283 nm shows a similar level of variation. The ground-based  $U$ -band measurements (effective central wavelength at 365.6 nm) also show a considerable level of variation, implying a potential role of the ground-based  $U$ -band imaging in tracking the temporal variations of the brightness. If its sampling frequency can be improved, e.g., by using more telescopes located in different longitudes, then it should also be possible to resolve the 4–5 day periodicity of the brightness (Del Genio & Rossow 1982; Lee et al. 2020). The ground-based  $U$ -band brightness shows temporal variations that are about a day or two ahead, e.g., the local brightness minimum is on September 1 and the local peak is on September 3–4, while the local minimum of the UVI data is on September 3 and the local peak is on September 4–5. This is consistent with the different viewing geometries: the morning side was



**Figure 8.** Time series of relative disk-integrated reflectivity [%] compared to the mean (or reference) phase curves at each wavelength. The solar phase angle is shown by the colors of the symbols (colorbar,  $0^{\circ}$ – $90^{\circ}$ ). The 283 and 365 nm data were taken by Akatsuki/UVI, which provided good temporal coverage.

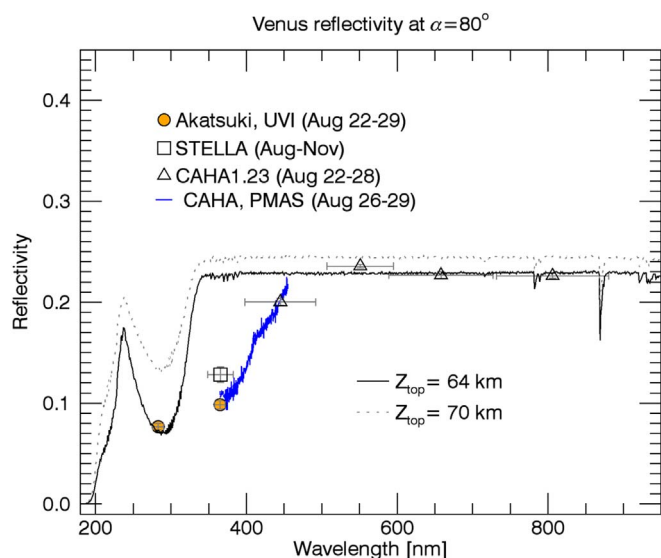
observed by the ground-based  $U$  imaging, and the noon-to-afternoon side by UVI (Figure 1(b)). It will take  $\sim 1$ – $2$  days for an air parcel to drift from the morning side to the afternoon side by means of the super-rotating background winds (Sánchez-Lavega et al. 2017; Horinouchi et al. 2018). The relative brightness in the  $B$  band shows a hint of temporal variation on August 22–28, especially the local minima on August 23 and 27. This variation may be a day ahead, compared to UVI, and caused by the unknown absorber, whose absorption extends toward the visible wavelength (Section 5.3). Future monitoring in the  $B$  band will be useful for quantifying its short-term variations. In the  $VRI$  bands, we do not expect to detect a short-term variability, because the impact of the unknown absorber diminishes at longer wavelengths (Section 5.3). A difference between the  $B$  and  $V$  magnitudes could be a proxy for monitoring the unknown absorber.

### 5.2. Mean Spectral Reflectivity and Comparison with Model Calculations

The mean reflectivity spectrum of the campaign is shown in Figure 9. All the imaging data are corrected to the  $80^{\circ}$  solar

phase angle, which is the value of the ground-based observations near the end of August (Figure 1(b)). This correction is done using the relative brightness [%] at the time of the observations and  $\bar{A}_{\text{disk-int}}(80^{\circ})$  (Equation (8)). The STELLA data point is the mean over a relatively long period (Section 3.4). The normalized reflectivity of the PMAS data at 445 nm (Section 3.5) is adjusted to match the  $B$ -band reflectivity (Section 3.3). The PMAS data do not require any solar phase angle correction, because the data were acquired at  $\alpha \sim 80^{\circ}$ . The horizontal error bars indicate the bandwidths of the imaging filters, and the vertical error bars the standard deviations over specific periods for each measurement, as indicated in the legends.

The modeled reflectivity at  $\alpha = 80^{\circ}$  is compared in Figure 9 with two cloud-top altitude assumptions, but without the unknown absorber. A large difference in the reflectivity between the calculations and the observations is present in wavelengths less than 460 nm. This difference is expected, as there is significant influence of the unknown absorber (Pérez-Hoyos et al. 2018). The calculated reflectivity with the 70 km cloud top is slightly brighter than the observed  $VRI$  reflectivity. We compared the reflectivity at the  $I$  band with the cloud-top altitudes in the range between 60 and 75 km, which control the



**Figure 9.** Comparison of the Venus reflectivity obtained from the four facilities during the campaign: Akatsuki/UVI (Section 3.1), STELLA/WiFSIP (Section 3.4), CAHA1.23/DLR-MKIII (Section 3.3), and CAHA3.5/PMAS (Section 3.5). The vertical error bars indicate standard deviations, while the horizontal error bars mean the bandwidth (FWHM). The calculated reflectivity is compared (Section 4), assuming two cloud-top altitudes without the unknown absorber (the solid and dashed lines).

impact of the Rayleigh scattering above the clouds (Figure 10). We find that the 64 km cloud-top altitude best fits the observed  $I$  reflectivity, and we use this cloud-top altitude in further modeling calculations. But we note that this configuration of the cloud-top altitude (64 km) should be considered as a tentative value, until we confirm the phase angle dependence using further observations.

The simulated reflectivity in Figure 9 shows that different cloud-top altitudes can significantly alter the depth of the  $\text{SO}_2$  absorption at 283 nm. Under the assumed  $\text{SO}_2$  abundance of 22.4 ppbv at 70 km (Lee et al. 2021), we can compare the two cloud-top altitude cases: 70 km and 64 km. (1) 70 km: the simulated spectrum results in shallow  $\text{SO}_2$  absorption. The difference between the observed 283 nm reflectivity and the model suggests considerable absorption by the unknown absorber. (2) 64 km: the simulated spectrum presents significant  $\text{SO}_2$  absorption. The unknown absorber’s contribution may not be necessary to explain the 283 nm reflectivity. We conclude that to retrieve the  $\text{SO}_2$  gas abundance and the absorption by the unknown absorber, it is necessary to have both good UV spectral coverage over the  $\text{SO}_2$  band and the reliable retrieval of the cloud-top altitudes. Such an analysis was successfully conducted, using UV spectrometer measurements, by Marcq et al. (2020), although the retrieval of the cloud-top altitudes was somewhat limited. More accurate retrievals are planned for a future mission, VenSpec-U, on board EnVision (Marcq et al. 2021). Also, future PHEBUS observations will contribute significantly to the determination of the  $\text{SO}_2$  gas abundance, by measuring the UV spectrum over the  $\text{SO}_2$  band.

The reflectivity around 365 nm shows a difference between the measurements by UVI and STELLA (Figure 9). The reason for the difference is not clearly understood, but it may be due to a possible absolute calibration issue with UVI (Section 3.1) and a retrieval error for the STELLA analysis, associated with the absence of the mean  $U$ -band phase curve (Section 3.4). In the

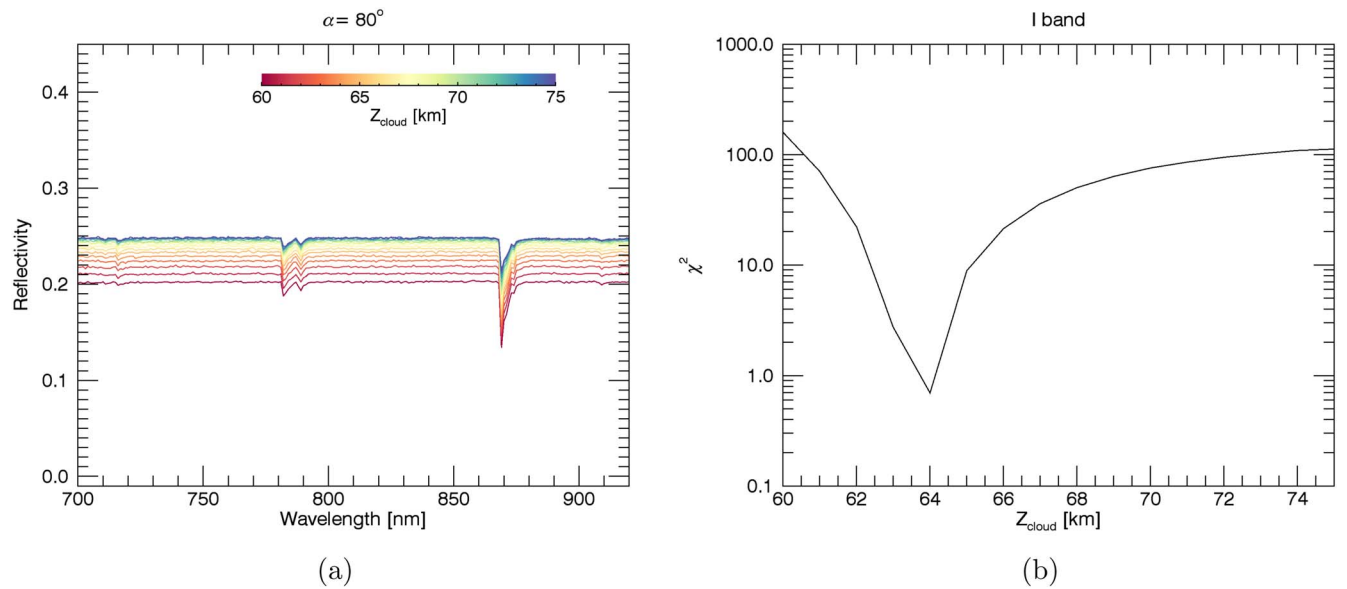
future, we will perform continuous star calibrations of UVI and Venus monitoring with STELLA to establish the mean  $U$ -band phase curve.

### 5.3. Unknown Absorber

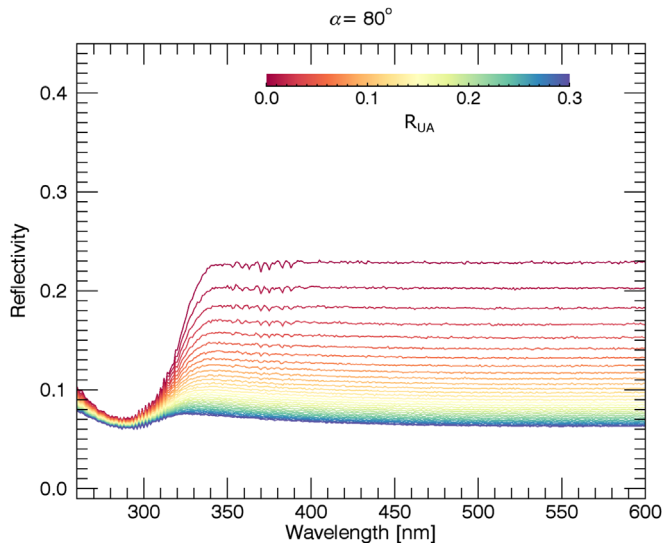
Figure 9 shows the difference in reflectivity between the simulations and observations over the  $\sim 350$ –460 nm range. This difference is due to the absorption by the unknown absorber in the clouds, which was not included in the simulations. In this section, we estimate the contribution of the unknown absorber using the PMAS spectral data, which provide the wavelength coverage down to the atmospheric cutoff in the UV. Our assumption on the unknown absorber is described in Section 4.2: reducing the SSA of the cloud aerosols by increasing  $R_{\text{UA}}$  within the 6 km layer right below the cloud top. The simulated reflectivity is wavelength-dependent, due to gaseous absorption and increasing Rayleigh scattering toward short wavelengths, as shown in Figure 11. We prepared a table of expected reflectivity as a function of wavelength ( $d\lambda = 1$  nm) and  $R_{\text{UA}}$  ( $dR_{\text{UA}} = 0.01$ ). Then we compared this table and the observed PMAS reflectivity (Figure 9) to find the corresponding absorption along wavelengths. This process was done in a two-dimensional interpolation: a linear interpolation along wavelengths and a least squares quadratic interpolation for the absorption at a fixed wavelength, to take into account the considerable nonlinear property with  $R_{\text{UA}}$ , as shown in Figure 11.

The resulting absorption spectrum is shown in Figure 12, as normalized optical depth to the maximum value in the 350–500 nm range. So the possible errors relating to the cloud-top altitude (Section 5.2) become irrelevant, and we can focus on the spectral shape of the absorption, to compare it with those of previous studies (Crisp 1986; Haus et al. 2016; Pérez-Hoyos et al. 2018). The high spectral resolution (gray curve) is convolved into a 1 nm grid (black curve), which is our model calculation resolution. The relative optical depth decreases with increasing wavelength, but more rapidly at  $\lambda < 410$  nm than at longer wavelengths, and it is expected to be close to zero at the  $V$  band. This wavelength dependence is consistent with the relative optical depth at low latitudes (Pérez-Hoyos et al. 2018). This is an expected result, considering the large portion of low latitudes in the equatorial view from the Earth (Figure 1(b)). This consistent spectral dependency also implies a negligible change in the chemical composition of the unknown absorber between the afternoon equatorial region in 2007 and the morning side in 2020.

Compared to the assumptions that were used in the solar heating rate calculations in Crisp (1986) and Haus et al. (2016), both observational data analyses suggest weaker absorption in the visible wavelength range than in the UV. This spectral shape of absorption may alter the solar heating rate near the cloud-top-level atmosphere. However, there are more factors that can affect the solar heating, such as the unknown absorber’s absolute abundance (Lee et al. 2019) and vertical location (Crisp 1986; Haus et al. 2016; Lee et al. 2021), and the cloud-top vertical structure (Lee et al. 2015b). Updating the heating rate is not within the scope of this study, but may be possible in future studies.



**Figure 10.** Relations between the reflectivity over the wavelengths of the *I* band and the cloud-top altitude ( $Z_{\text{cloud}}$ ). (a) Variations of the calculated reflectivity according to  $Z_{\text{cloud}}$  that is changed between 60 and 75 km. (b)  $\chi^2$  to fit the observed *I*-band reflectivity as a function of  $Z_{\text{cloud}}$ .

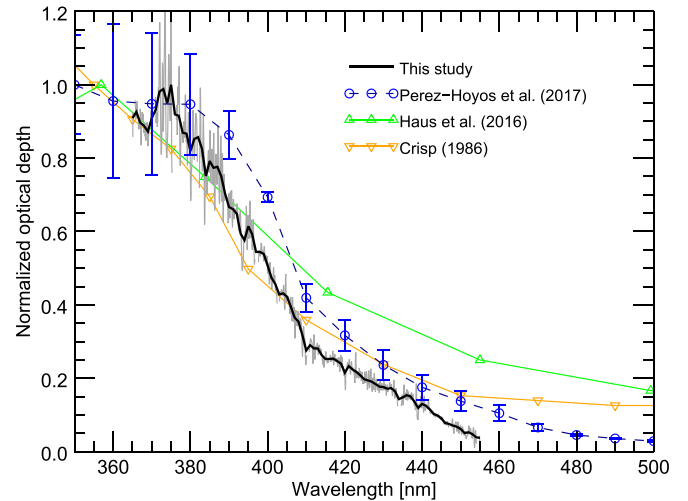


**Figure 11.** Simulated reflectivity at  $\alpha = 80^\circ$  with a range of  $R_{\text{UA}}$  from 0.0 to 0.3 (see Section 4.2). This assumes the best fit of the cloud top in Figure 10(b) (64 km). The unknown absorber is assumed to be within the 6 km thickness layer, whose middle is located 3 km below the cloud-top level (Lee et al. 2021), i.e., 58–64 km. Within this layer, the SSA of the cloud aerosols is reduced by  $R_{\text{UA}}$ .

## 6. Summary and Perspective on Future Campaigns

Our dayside observation campaign was conducted with the PHEBUS spectrometer on board BepiColombo and the UVI camera on board Akatsuki to better understand the UV absorbers in the Venusian clouds. Our campaign was designed to cover a broad wavelength range, from 52 to 1700 nm, thanks to Earth-bound observation facilities. Despite the fact that our data analysis could eventually only utilize the data between 283 and 800 nm (Section 2), we achieved the following goals and insights:

1. We successfully accomplished the Venus observation campaign using multiple ground- and space-based facilities almost simultaneously.



**Figure 12.** Relative optical depth of the unknown absorber (normalized to the maximum in the 350–500 nm range). The required absorption to match the PMAS data is shown with the gray line (Section 5.3), and its convolution (FWHM = 1 nm) is shown with the black line. A previous observational data analysis (Pérez-Hoyos et al. 2018) is shown for comparison (blue circles). Assumptions that were applied for the solar heating rate calculations (upward/downward triangles; Crisp 1986; Haus et al. 2016) are shown together.

2. Despite the challenging brightness of the target (too bright), we managed to acquire high-quality data.
3. The PHEBUS team was able to establish a robust observation strategy for making successful Venus observations at future opportunities, e.g., in 2022 June and July.
4. Using the campaign data in the 283–800 nm range, we retrieved the relative optical depth of the unknown absorber on the morning-side disk. Our result is consistent with the previous report using the data acquired in 2007 over the afternoon equatorial region (Pérez-Hoyos et al. 2018).
5. We plan future campaigns to retrieve both the  $\text{SO}_2$  gas abundance and the absorption by the unknown absorber in the 180–450 nm range, using data acquired by PHEBUS (180–320 nm), UVI (283 and 365 nm), and ground-based telescopes (350–800 nm).

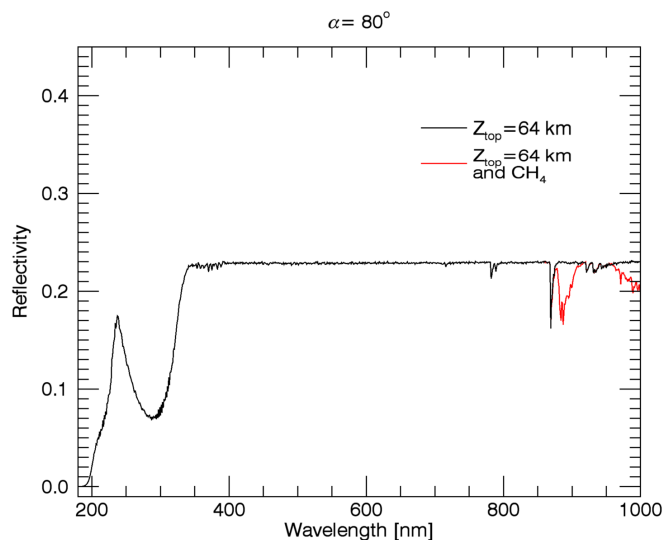


6. We established that flux measurements at the *VRI* bands can provide a constraint on the cloud configuration to generate the simulated reflectivity. We will continue *VRI* imaging in future campaigns.
7. The *U*-band phase curve of Venus is poorly defined. We plan to continue the *U*-band imaging to define a mean phase curve.
8. Through the ground-based *U*-band measurements, it may be possible to track the temporal variability of Venus's reflectivity, in addition to space-based measurements.
9. Akatsuki's UV imaging is an excellent reference for comparing short-term variations.
10. PMAS observation and flux measurements in the *B*-band will be repeated in our future campaigns to understand the possible temporal variations of the unknown absorber.

This research used data collected at the Centro Astronómico Hispano-Alemán (CAHA) at Calar Alto, operated jointly by Junta de Andalucía and Consejo Superior de Investigaciones Científicas (IAA-CSIC). This research has made use of the integral field spectroscopy data reduction tool p3d, which is provided by the Leibniz-Institut für Astrophysik Potsdam (AIP). Akatsuki/UVI data are publicly available at the JAXA archive website, DARTS (<http://darts.isas.jaxa.jp/>), and the NASA archive website, PDS (<https://pds.nasa.gov/>). UVI Level 3 products (13bx) were used in this study (Murakami et al. 2018). This study used the TSIS-1 SIM data (Version 06, doi:10.25810/y9f8-ff85). M.K. and O.E. thank the TÜBİTAK National Observatory for partial support in using the T100 telescope, with project number 20CT100-1688. R. H. and A.S.L. have been supported by the Spanish project PID2019-109467GB-I00 (MINECO/FEDER, UE) and Grupos Gobierno Vasco IT-1366-19. P.K. and M.S. acknowledge support from grant LTT-20015.

### Appendix Spectral Signature of Methane (CH<sub>4</sub>)

At first, we assumed possible methane gas in the model calculations (Section 4.1). But later, we found that its spectral signature should be clear to detect with remote observations (Figure 13). We excluded methane from the results in this



**Figure 13.** Simulated Venus reflectivity for two cases: without CH<sub>4</sub> (black) and with CH<sub>4</sub> (red). The latter case assumed the vertical mixing ratio of methane in Figure 6(c).

manuscript (Section 5). The confirmation of the possible methane may be a subject of future observation projects.

### ORCID iDs

Yeon Joo Lee <https://orcid.org/0000-0002-4571-0669>  
 Antonio García Muñoz <https://orcid.org/0000-0003-1756-4825>  
 Atsushi Yamazaki <https://orcid.org/0000-0001-6468-6812>  
 Eric Quémerais <https://orcid.org/0000-0001-5376-2242>  
 Stefano Mottola <https://orcid.org/0000-0002-0457-3872>  
 Stephan Hellmich <https://orcid.org/0000-0003-3997-3363>  
 Martin Roth <https://orcid.org/0000-0003-2451-739X>  
 Eulalia Gallego-Cano <https://orcid.org/0000-0002-7452-1496>  
 Kei Masunaga <https://orcid.org/0000-0001-9704-6993>  
 Ricardo Hueso <https://orcid.org/0000-0003-0169-123X>  
 Petr Kabáth <https://orcid.org/0000-0002-1623-5352>  
 Agustín Sánchez-Lavega <https://orcid.org/0000-0001-7234-7634>  
 Myung-Jin Kim <https://orcid.org/0000-0002-4787-6769>  
 Valeria Mangano <https://orcid.org/0000-0002-9903-4053>  
 Shigeto Watanabe <https://orcid.org/0000-0002-3058-0689>  
 Manabu Yamada <https://orcid.org/0000-0003-0726-6592>  
 Takehiko Satoh <https://orcid.org/0000-0001-9071-5808>  
 Masataka Imai <https://orcid.org/0000-0001-8543-6556>  
 Juan Cabrera <https://orcid.org/0000-0001-6653-5487>

### References

- Acton, C. H. 1996, *P&SS*, **44**, 65  
 Bahou, M., Chung, C.-Y., Lee, Y.-P., et al. 2001, *ApJL*, **559**, L179  
 Bains, W., Petkowski, J. J., Rimmer, P. B., & Seager, S. 2021, *PNAS*, **118**, e2110889118  
 Barker, E. S., Woodman, J. H., Perry, M. A., Hapke, B. A., & Nelson, R. 1975, *JAts*, **32**, 1205  
 Belyaev, D. A., Montmessin, F., Bertaux, J.-L., et al. 2012, *Icar*, **217**, 740  
 Bierson, C. J., & Zhang, X. 2020, *JGRE*, **125**, e06159  
 Bohlin, R. C., Gordon, K. D., & Tremblay, P. E. 2014, *PASP*, **126**, 711  
 Burkholder, J. B., Sander, S. P., Abbatt, J., et al. 2019, Chemical Kinetics and Photochemical Data for Use in Atmospheric Studies, Evaluation No. 19 (Pasadena, CA: JPL)  
 Chance, K., & Kurucz, R. L. 2010, *JQST*, **111**, 1289  
 Chassefière, E., Maria, J. L., Goutail, J. P., et al. 2010, *P&SS*, **58**, 201  
 Connes, P., Connes, J., Benedict, W. S., & Kaplan, L. D. 1967, *ApJ*, **147**, 1230  
 Crisp, D. 1986, *Icar*, **67**, 484  
 Del Genio, A. D., & Rossow, W. B. 1982, *Icar*, **51**, 391  
 Del Genio, A. D., & Rossow, W. B. 1990, *JAts*, **47**, 293  
 Donahue, T. M., & Hodges, R. R. 1993, *GeoRL*, **20**, 591  
 Ducati, J. R. 2002, *yCat*, **2237**, 0  
 Encrenaz, T., Greathouse, T. K., Marçq, E., et al. 2019, *A&AC*, **623**, A70  
 Esposito, L. W. 1980, *JGR*, **85**, 8151  
 Esposito, L. W., Copley, M., Eckert, R., et al. 1988, *JGR*, **93**, 5267  
 Feng, R., Cooper, G., & Brion, C. E. 2000a, *CP*, **252**, 359  
 Feng, R., Cooper, G., Burton, G. R., Brion, C., & Avaldi, L. 1999, *CP*, **240**, 371  
 Feng, R., Cooper, G., Sakai, Y., & Brion, C. E. 2000b, *CP*, **255**, 353  
 Fillion, J. H., Ruiz, J., Yang, X. F., et al. 2004, *JChPh*, **120**, 6531  
 García Muñoz, A. 2015, *IJAsB*, **14**, 379  
 Carrión-González, Ó., García Muñoz, A., Cabrera, J., et al. 2020, *A&A*, **640**, A136  
 García Muñoz, A., & Mills, F. P. 2015, *A&A*, **573**, A72  
 Carrión-González, Ó., García Muñoz, A., Santos, N. C., et al. 2021, *A&A*, **655**, A92  
 Gillon, M., Smalley, B., Hebb, L., et al. 2009, *A&A*, **496**, 259  
 Gordon, I. E., Rothman, L. S., Hill, C., et al. 2017, *JQST*, **203**, 3  
 Gray, R. O., Corbally, C. J., Garrison, R. F., McFadden, M. T., & Robinson, P. E. 2003, *AJ*, **126**, 2048  
 Grosch, H., Fateev, A., & Clausen, S. 2015, *JQST*, **154**, 28  
 Hapke, B. 2012, Theory of Reflectance and Emittance Spectroscopy (2nd edn.; Cambridge: Cambridge Univ. Press)

- Hartering, K. T., Nord, S., & Monkhouse, P. B. 2000, *ApPhB*, **70**, 133
- Haus, R., Kappel, D., Tellmann, S., et al. 2016, *Icar*, **272**, 178
- Heays, A. N., Bosman, A. D., & van Dishoeck, E. F. 2017, *A&A*, **602**, A105
- Helou, Z. E., Churassy, S., Wannous, G., Bacis, R., & Boursey, E. 2005, *JChPh*, **122**, 244311
- Hermans, C., Vandaele, A. C., & Fally, S. 2009, *JQRST*, **110**, 756
- Horinouchi, T., Kouyama, T., Lee, Y. J., et al. 2018, *EP&S*, **70**, 10
- Huang, X., Schwenke, D. W., Freedman, R. S., & Lee, T. J. 2017, *JQRST*, **203**, 224
- Huestis, D. L., & Berkowitz, J. 2011, in *Advances in Geosciences. Volume 25: Planetary Science*, ed. K. Satake et al. (Singapore: World Scientific), 229
- Hummel, J. R., Shettle, E. P., & Longtin, D. R. 1988, A new background stratospheric aerosol model for use in atmospheric radiation models, Technical rept. ADA210110, Defense Technical Information Center 70, <https://apps.dtic.mil/sti/citations/ADA210110>
- Ignatiev, N. I., Titov, D. V., Piccioni, G., et al. 2009, *JGRE*, **114**, E00B43
- Imai, M., Kouyama, T., Takahashi, Y., et al. 2019, *JGRE*, **124**, 2635
- Irvine, W. M., Simon, T., Menzel, D. H., et al. 1968, *AJ*, **73**, 251
- Jessup, K.-L., Marcq, E., Bertaux, J.-L., et al. 2020, *Icar*, **335**, 113372
- Jessup, K. L., Marcq, E., Mills, F., et al. 2015, *Icar*, **258**, 309
- Johnson, N. M., & de Oliveira, M. R. R. 2019, *E&SS*, **6**, 1299
- Kabáth, P., Skarka, M., Sabotta, S., et al. 2020, *PASP*, **132**, 035002
- Keller-Rudek, H., Moortgat, G. K., Sander, R., & Sørensen, R. 2013, *ESSD*, **5**, 365
- Knollenberg, R. G., & Hunten, D. M. 1980, *JGR*, **85**, 8039
- Knuckles, C. F., Sinton, M. K., & Sinton, W. M. 1961, *LowOB*, **5**, 153
- Koen, C., Kilkenny, D., van Wyk, F., & Marang, F. 2010, *MNRAS*, **403**, 1949
- Krasnopolsky, V. A. 2018, *Icar*, **299**, 294
- Langeveld, A. B., Madhusudhan, N., Cabot, S. H. C., & Hodgkin, S. T. 2021, *MNRAS*, **502**, 4392
- Lee, Y. J., García Muñoz, A., Imamura, T., et al. 2020, *NatCo*, **11**, 5720
- Lee, Y. J., García Muñoz, A., Yamazaki, A., et al. 2021, *GeoRL*, **48**, e90577
- Lee, Y. J., Imamura, T., Schröder, S. E., & Marcq, E. 2015a, *Icar*, **253**, 1
- Lee, Y. J., Jessup, K.-L., Perez-hoyos, S., et al. 2019, *AJ*, **158**, 126
- Lee, Y. J., Sagawa, H., Haus, R., et al. 2016, *JGRE*, **121**, 1737
- Lee, Y. J., Titov, D. V., Ignatiev, N. I., et al. 2015b, *P&SS*, **113**, 298
- Lee, Y. J., Titov, D. V., Tellmann, S., et al. 2012, *Icar*, **217**, 599
- Lee, Y. J., Yamazaki, A., Imamura, T., et al. 2017, *AJ*, **154**, 44
- Limão-Vieira, P., Ferreira da Silva, F., Almeida, D., et al. 2015, *JChPh*, **142**, 064303
- Limaye, S. S., Mogul, R., Smith, D. J., et al. 2018, *AsBio*, **18**, 1181
- Mallama, A., Krobusek, B., & Pavlov, H. 2017, *Icar*, **282**, 19
- Manatt, S. L., & Lane, A. L. 1993, *JQSRT*, **50**, 267
- Mangano, V., Dósa, M., Fränz, M., et al. 2021, *SSRv*, **217**, 23
- Marcq, E., Baggio, L., Lefèvre, F., et al. 2019, *Icar*, **319**, 491
- Marcq, E., Belyaev, D., Montmessin, F., et al. 2011, *Icar*, **211**, 58
- Marcq, E., Bertaux, J.-L., Montmessin, F., & Belyaev, D. 2013, *NatGe*, **6**, 25
- Marcq, E., Jessup, K.-L., Baggio, L., et al. 2020, *Icar*, **335**, 113368
- Marcq, E., Montmessin, F., Lasue, J., et al. 2021, *AdSpR*, **68**, 275
- Markiewicz, W. J., Titov, D. V., Limaye, S. S., et al. 2007, *Natur*, **450**, 633
- Mason, N. J., Gingell, J. M., Davies, J. A., et al. 1996, *JPhB*, **29**, 3075
- Meadows, V. S., & Crisp, D. 1996, *JGR*, **101**, 4595
- Mendikoa, I., Sánchez-Lavega, A., Pérez-Hoyos, S., et al. 2016, *PASP*, **128**, 035002
- Mills, F. P., Esposito, L. W., & Yung, Y. L. 2007, *GMS*, **176**, 73
- Mishchenko, M. I., Travis, L. D., & Lacis, A. A. 2002, *Scattering, Absorption, and Emission of Light by Small Particles* (Cambridge: Cambridge Univ. Press)
- Molina, L. T., Lamb, J. J., & Molina, M. J. 1981, *GeoRL*, **8**, 1008
- Mota, R., Parafita, R., Giuliani, A., et al. 2005, *CPL*, **416**, 152
- Murakami, S., Ogohara, K., Takagi, M., et al. 2018, Inst. of Space and Astronautical Science, Japan Aerospace Exploration Agency
- Na, C. Y., Esposito, L. W., & Skinner, T. E. 1990, *JGR*, **95**, 7485
- Nakamura, M., Imamura, T., Ishii, N., et al. 2016, *EP&S*, **68**, 75
- Nara, Y., Yoshikawa, I., Yoshioka, K., et al. 2018, *Icar*, **307**, 207
- Pei, L., Min, Q., Du, Y., et al. 2019, *JGRD*, **124**, 14,310
- Pérez-Hoyos, S., Sánchez-Lavega, A., García-Muñoz, A., et al. 2018, *JGRE*, **123**, 145
- Petrova, E. V. 2018, *Icar*, **306**, 163
- Phillips, L. F. 1981, *JPhCh*, **85**, 3994
- Pollack, J. B., Dalton, J. B., Grinspoon, D., et al. 1993, *Icar*, **103**, 1
- Pollack, J. B., Toon, O. B., Whitten, R. C., et al. 1980, *JGR*, **85**, 8141
- Quémerais, E., Chaufray, J.-Y., Koutroumpa, D., et al. 2020, *SSRv*, **216**, 67
- Ranjan, S., Schwieterman, E. W., Harman, C., et al. 2020, *ApJ*, **896**, 148
- Rosales-Ortega, F. F., Kennicutt, R. C., Sánchez, S. F., et al. 2010, *MNRAS*, **405**, 735
- Ross, F. E. 1928, *ApJ*, **68**, 57
- Roth, M. M., Kelz, A., Fechner, T., et al. 2005, *PASP*, **117**, 620
- Sánchez-Lavega, A., Lebonnois, S., Imamura, T., Read, P., & Luz, D. 2017, *SSRv*, **212**, 1541
- Sandin, C., Becker, T., Roth, M. M., et al. 2010, *A&A*, **515**, A35
- Satoh, T., Ohtsuki, S., Iwagami, N., et al. 2015, *Icar*, **248**, 213
- Seiff, A., Schofield, J. T., Kliore, A. J., Taylor, F. W., & Limaye, S. S. 1985, *AdSpR*, **5**, 3
- Sneep, M., & Ubachs, W. 2005, *JQSRT*, **92**, 293
- Southworth, J., Hinse, T. C., Jørgensen, U. G., et al. 2009, *MNRAS*, **396**, 1023
- Smolovsky, L. A., Fry, P. M., Baines, K. H., & Dowling, T. E. 2001, *Icar*, **149**, 435
- Stark, G., Yoshino, K., Smith, P. L., & Ito, K. 2007, *JQRST*, **103**, 67
- Stepien, K., & Geyer, E. 1996, *A&AS*, **117**, 83
- Strassmeier, K. G., Granzer, T., Weber, M., et al. 2010, *AdAst*, **2010**, 970306
- Titov, D. V., Bullock, M. A., Crisp, D., et al. 2007, *GMS*, **176**, 121
- Titov, D. V., Ignatiev, N. I., McGouldrick, K., Wilquet, V., & Wilson, C. F. 2018, *SSRv*, **214**, 126
- Titov, D. V., Markiewicz, W. J., Ignatiev, N. I., et al. 2012, *Icar*, **217**, 682
- Vandaele, A. C., Hermans, C., & Fally, S. 2009, *JQRST*, **110**, 2115
- Venot, O., Bénilan, Y., Fray, N., et al. 2018, *A&A*, **609**, A34
- von Zahn, U., & Moroz, V. I. 1985, *AdSpR*, **5**, 173
- Willmer, C. N. A. 2018, *ApJS*, **236**, 47
- Wilson, E. M., Wenger, J. C., & Venables, D. S. 2016, *JQRST*, **170**, 194
- Wright, W. H. 1927, *PASP*, **39**, 220
- Wu, C. Y. R., & Chen, F. Z. 1998, *JQRST*, **60**, 17
- Wytenbach, A., Ehrenreich, D., Lovis, C., Udry, S., & Pepe, F. 2015, *A&A*, **577**, A62
- Yamazaki, A., Yamada, M., Lee, Y. J., et al. 2018, *EP&S*, **70**, 23
- Yoshikawa, I., Yoshioka, K., Murakami, G., et al. 2014, *SSRv*, **184**, 237
- Zasova, L. V., Krasnopolskii, V. A., & Moroz, V. I. 1981, *AdSpR*, **1**, 13